



<b>Publication Year</b>	2021
<b>Acceptance in OA</b>	2022-03-14T12:53:43Z
<b>Title</b>	Light, medium-weight, or heavy? The nature of the first supermassive black hole seeds
<b>Authors</b>	SASSANO, FEDERICA, Schneider, Raffaella, VALIANTE, ROSA, Inayoshi, Kohei, Chon, Sunmyon, Omukai, Kazuyuki, Mayer, Lucio, Capelo, Pedro R.
<b>Publisher's version (DOI)</b>	10.1093/mnras/stab1737
<b>Handle</b>	<a href="http://hdl.handle.net/20.500.12386/31563">http://hdl.handle.net/20.500.12386/31563</a>
<b>Journal</b>	MONTHLY NOTICES OF THE ROYAL ASTRONOMICAL SOCIETY
<b>Volume</b>	506

# Light, medium-weight, or heavy? The nature of the first supermassive black hole seeds

Federica Sassano<sup>1,2</sup>★, Raffaella Schneider<sup>1,2,3</sup>, Rosa Valiante<sup>1,2,3</sup>, Kohei Inayoshi<sup>4</sup>,  
Sunmyon Chon<sup>5</sup>, Kazuyuki Omukai<sup>5</sup>, Lucio Mayer<sup>6</sup> and Pedro R. Capelo<sup>6</sup>

<sup>1</sup>Dipartimento di Fisica, Sapienza, Università di Roma, Piazzale Aldo Moro 5, I-00185 Roma, Italy

<sup>2</sup>INFN, Sezione di Roma I, P.le Aldo Moro 2, I-00185 Roma, Italy

<sup>3</sup>INAF/Osservatorio Astronomico di Roma, Via di Frascati 33, I-00078 Monte Porzio Catone, Italy

<sup>4</sup>Kavli Institute for Astronomy and Astrophysics, Peking University, Beijing 100871, China

<sup>5</sup>Astronomical Institute, Graduate School of Science, Tohoku University, Aoba, Sendai 980-8578, Japan

<sup>6</sup>Center for Theoretical Astrophysics and Cosmology, Institute for Computational Science, University of Zurich, Winterthurerstrasse 190, CH-8057 Zürich, Switzerland

Accepted 2021 June 14. Received 2021 June 14; in original form 2020 August 3

## ABSTRACT

Observations of hyper-luminous quasars at  $z > 6$  reveal the rapid growth of supermassive black holes (SMBHs  $> 10^9 M_\odot$ ) whose origin is still difficult to explain. Their progenitors may have formed as remnants of massive, metal-free stars (light seeds), via stellar collisions (medium-weight seeds) and/or massive gas clouds direct collapse (heavy seeds). In this work, we investigate for the first time the relative role of these three seed populations in the formation of  $z > 6$  SMBHs within an Eddington-limited gas accretion scenario. To this aim, we implement in our semi-analytical data-constrained model a statistical description of the spatial fluctuations of Lyman–Werner (LW) photodissociating radiation and of metal/dust enrichment. This allows us to set the physical conditions for black hole seeds formation, exploring their relative birth rate in a highly biased region of the Universe at  $z > 6$ . We find that the inclusion of medium-weight seeds does not qualitatively change the growth history of the first SMBHs: although less massive seeds ( $< 10^3 M_\odot$ ) form at a higher rate, the mass growth of a  $\sim 10^9 M_\odot$  SMBH at  $z < 15$  is driven by efficient gas accretion (at a sub-Eddington rate) on to its heavy progenitors ( $10^5 M_\odot$ ). This conclusion holds independently of the critical level of LW radiation and even when medium-weight seeds are allowed to form in higher metallicity galaxies, via the so-called supercompetitive accretion scenario. Our study suggests that the genealogy of  $z \sim 6$  SMBHs is characterized by a rich variety of BH progenitors, which represent only a small fraction ( $< 10$ – $20$  per cent) of all the BHs that seed galaxies at  $z > 15$ .

**Key words:** black hole physics – galaxies: evolution – galaxies: high-redshift – quasars: supermassive black holes.

## 1 INTRODUCTION

Starting from their first detection by Fan et al. (2002, 2003), more than 100 supermassive black holes (SMBHs), with masses  $\geq 10^9 M_\odot$ , have been observed at  $z > 6$  as bright quasars (e.g. Willott et al. 2010; Bañados et al. 2016; Jiang et al. 2016; Matsuoka et al. 2019; Yang et al. 2020). The most massive among this high-redshift sample is the hyper-luminous quasar SDSS J0100+2802, with a mass of  $1.2 \times 10^{10} M_\odot$  at  $z = 6.3$  (Wu et al. 2015). The three most distant ones are J0313-1806 (Wang et al. 2021), with an SMBH mass of  $1.6 \times 10^9 M_\odot$ , ULAS J1342+0928 (Bañados et al. 2018), with an SMBH mass of  $7.8 \times 10^8 M_\odot$  detected at  $z = 7.54$ , and the recently reported *Pōniuā’ena* (J1007+2115, Yang et al. 2020), with an SMBH mass of  $1.5 \times 10^9 M_\odot$  at  $z = 7.52$ , when the Universe was only 0.69 Gyr old. The estimated SMBH masses imply that common mechanisms of Eddington-limited gas accretion on to stellar mass black holes fail to provide a fast enough BH mass growth at these early cosmic epochs (see, for a recent review, Inayoshi, Visbal & Haiman 2019).

A possible scenario is to consider Population III (Pop III) stellar remnants, or *light seeds*, as progenitors of SMBHs. Pop III stars are expected to form around  $z \sim 20$ – $30$  (Bromm 2013), in the first collapsed structures, *minihaloes* with virial temperatures  $T_{\text{vir}} < 10^4$  K where the collapse of primordial gas is driven by molecular hydrogen cooling. While hydrodynamical models assuming spherical symmetry (Omukai & Nishi 1998; Omukai, Hosokawa & Yoshida 2010) and those starting from cosmological initial conditions (Yoshida, Omukai & Hernquist 2008) show a remarkable agreement in describing the early collapse phase and the formation of the central hydrostatic core (see also Bromm 2013 and references therein), large uncertainties still remain on the evolution of the post-collapse phase, when disc fragmentation, protostellar evolution, and radiative feedback become important (Omukai & Palla 2003; Hosokawa et al. 2011; see for a review Greif 2015). The resulting Pop III mass distribution is generally found to be top heavy, with stellar masses ranging from a few tens to several hundreds of solar masses (Hirano et al. 2014, 2015; Hosokawa et al. 2016) and a non-negligible fraction of stars formed in binary or multiple systems (Sugimura et al. 2020). Independent constraints on the Pop III initial mass function (IMF) come from stellar archaeology studies (see Frebel & Norris 2015

\* E-mail: federica.sassano@uniroma1.it

for a thorough review). The low-metallicity tail of the metallicity distribution function of Galactic halo stars and their observed large carbon-to-iron surface abundance ratios appear to be consistent with models where Pop III stars form in the range  $[10\text{--}300]M_{\odot}$  with a characteristic mass of  $20M_{\odot}$  (de Bressana et al. 2017) and where the early chemical enrichment is dominated by the explosion of faint supernovae (SNe; Marassi et al. 2014). Even assuming that BH remnants of this first stellar generation can extend to masses of a few 100s of  $M_{\odot}$ , these light seeds can grow in mass to form SMBHs at  $z > 6$  only if they accrete gas at super-Eddington rates, even in short and intermittent phases (Pezzulli, Valiante & Schneider 2016; Pezzulli et al. 2017). Recently, simulations have become capable of studying supercritical accretion in realistic astrophysical environments, assuming slim accretion discs (Sądowski 2009; Madau, Haardt & Dotti 2014, Sądowski and Narayan 2016, Lupi et al. 2016), or spherically accreting envelopes, without dynamically important angular momentum (Inayoshi, Haiman & Ostriker 2016; Takeo, Inayoshi & Mineshige 2020). The question is whether the high gas densities required to sustain super-Eddington accretion can be found in light seed environments at high redshifts (see for a critical discussion Mayer & Bonoli 2019).

An alternative scenario to grow SMBHs in the early Universe is to start from *heavy seeds*,  $\sim 10^5 M_{\odot}$  BHs formed from the collapse of supermassive stars (SMSs; Omukai 2001; Bromm & Loeb 2003; Wise, Turk & Abel 2008; Regan & Haehnelt 2009; Shang, Bryan & Haiman 2010; Hosokawa, Omukai & Yorke 2012; Latif et al. 2013; Inayoshi, Omukai & Tasker 2014; Regan, Johansson & Wise 2014; Becerra et al. 2015; Chon et al. 2016; Latif, Schleicher & Hartwig 2016; Becerra et al. 2018; Maio et al. 2019; Wise et al. 2019a) or in gas-rich galaxy mergers (Mayer et al. 2015; Mayer 2017; Mayer & Bonoli 2019). In the first case, gas cooling and fragmentation must be avoided to form a single supermassive object. For this reason, *heavy seeds* are expected to form in pristine haloes with virial temperatures  $T_{\text{vir}} \geq 10^4 K$ , the so-called *atomic cooling haloes*, where fragmentation is avoided because of the lack of metals and molecular hydrogen cooling is suppressed by a sufficiently strong radiation field in the Lyman–Werner (LW) band (Omukai, Schneider & Haiman 2008; Dijkstra, Ferrara & Mesinger 2014; Sugimura, Omukai & Inoue 2014; Wolcott-Green, Haiman & Bryan 2017; Wolcott-Green, Haiman & Bryan 2020) or by dynamical heating caused by rapidly growing dark matter (DM) haloes (Mayer et al. 2015; Wise et al. 2019a). In addition to avoiding fragmentation, very high accretion rates, with  $\dot{M} > 0.01 M_{\odot} \text{ yr}^{-1}$ , are required to reduce radiative feedback from the growing protostar on to the accretion flow (Hosokawa et al. 2012; Chon, Hosokawa & Yoshida 2018; Matsukoba et al. 2019).

Finally, a third scenario foresees the formation of BH seeds with mass  $\sim 10^3 M_{\odot}$ , also called intermediate mass black holes, which we will refer to as *medium-weight seeds*. Their formation is expected to occur through run-away stellar collisions in dense star clusters (Omukai et al. 2008; Volonteri 2010; Devecchi et al. 2012; Katz, Sijacki & Haehnelt 2015; Sakurai et al. 2017; Stone, Küpper & Ostriker 2017; Reinoso et al. 2018; Tagawa, Haiman & Kocsis 2020) or BHs runaway mergers (Davies, Miller & Bellovary 2011, Lupi et al. 2014). These are supposed to originate in atomic cooling haloes where the gas initially undergoes an almost isothermal collapse, similar to the early formation phase of *heavy seeds*. Hence, their formation requires conditions similar to the ones discussed above, lack of metal fine structure line, and  $H_2$  cooling. However, a dense star cluster may form provided that dust cooling drives fragmentation in the late phase of the collapse (Omukai et al. 2008). It is important to stress that this simple picture may be significantly affected by the

dynamics of the infalling gas. Indeed, Chon & Omukai (2020) show that, in the absence of  $H_2$  cooling, although dust cooling promotes the formation of a few thousand low-mass stars, the strong accreting flow preferentially feeds the central star which grows supermassive. Hence, in this *supercompetitive accretion* (SCA) mode, the formation of *heavy seeds* may continue even in moderately enriched haloes, and *medium-weight seeds* form only when metal line cooling starts to decrease the gas temperature, at  $Z \sim 10^{-3} Z_{\odot}$ , lowering the accretion rate.

The importance of *medium-weight seeds* is not only related to SMBH genealogy, but has a number of additional implications in astrophysics. Medium-weight seeds would extend the correlation between the stellar and nuclear black hole masses to dwarf galaxies (Greene et al. 2010; Safonova & Shastri 2010; Reines & Volonteri 2015; Mezcua et al. 2018), they could explain the existence of ultraluminous X-ray sources (Miller, Fabian & Miller 2004; Fritze, Wright & Kilgard; Barrows, Mezcua & Comerford 2019; Shen 2019; Baldassare et al. 2020), and are necessary to prevent tidal disruption events in young star clusters observed in the galactic nucleus (Kim, Figer & Morris 2004). These  $\sim 10^3 M_{\odot}$  BHs will be targeted by future third-generation gravitational telescopes, such as the laser interferometer space antenna (Coleman Miller & Hamilton 2002; Sesana et al. 2005; Amaro-Seoane & Santamaria 2010; Kremer et al. 2019, Dayal et al. 2019), but recent observations (Ballone, Mapelli & Pasquato 2018; Barack et al. 2019; Nguyen et al. 2019; Takekawa et al. 2019; Woo et al. 2019) have found evidence of their existence in the Local Universe.

In this work, we aim at assessing the relative importance of *light*, *medium-weight*, and *heavy seeds*, in the mass growth histories of  $z \sim 6$  SMBHs. To this aim, we have largely improved our original seeding prescription described in Valiante et al. (2016b, 2018a) in order to investigate the formation sites of all these three families of BH seeds in the cosmological evolution of a typical  $z \sim 6$  SMBH and its host galaxy. In particular, we present here a more physical treatment of the inhomogeneous radiative and chemical feedback. We quantify the statistical distributions of all BH seeds in several independent simulations of the final SMBH, and explore how these are impacted by assuming different conditions (critical LW flux, metallicity, and dust-to-gas mass ratios) for their formation.

The paper is organized as follows. In Section 2, we briefly describe the semi-analytical model adopted in our analysis. Section 3 presents the new features implemented for this work, i.e. *the medium-weight seed* formation scenario (Sections 3.1 and 3.2) and the inhomogeneous treatment of metal enrichment and radiative LW flux (Section 3.3). In Section 4, we describe the main results, which will be discussed and summarized in Sections 5 and 6.

For our analysis, we will assume a *Planck* Cosmology with  $\Omega_m = 0.314$ ,  $\Omega_{\Lambda} = 0.686$ ,  $n_s = 0.96$ ,  $h = 0.674$  and  $\sigma_8 = 0.834$  from Ade et al. (2014).

## 2 DESCRIPTION OF THE MODEL

Here, we summarize the main features of the semi-analytical, data constrained model, GAMETE/QSOdust (GQd) developed to simulate the cosmological build-up of a  $z \sim 6$  SMBH and its host galaxy (Valiante et al. 2011, 2014, 2016b).

GQd follows the co-evolution of nuclear BHs and their host galaxies and, at the same time, the metal and dust enrichment of their interstellar medium (ISM), in a cosmological context. For this reason, GQd is suitable to investigate the birth environments of BH seeds in high-redshift galaxies, their subsequent mass growth through gas accretion and mergers, and their relative contribution to the final

**Table 1.** Free parameters of the Reference and SCA models.  $\epsilon_{\text{quiesc}}$  is the star formation efficiency (see equation 2),  $\epsilon_{w,\text{SN}}$  is the SN-driven wind efficiency (see equation 7),  $\alpha_{\text{BH}}$  quantifies the efficiency of BH accretion (see equation 9), and  $\epsilon_{w,\text{AGN}}$  is the BH-driven wind efficiency (see equation 11). For each set of models, these values have been calibrated to reproduce the observed properties of the  $z = 6.42$  QSO J1148 and its host galaxy (see Valiante et al. 2016b).

Model	$\epsilon_{\text{quiesc}}$	$\epsilon_{w,\text{SN}}$	$\alpha_{\text{BH}}$	$\epsilon_{w,\text{AGN}}$
Reference	0.1	$1.6 \times 10^{-3}$	150	$2.5 \times 10^{-3}$
SCA	0.1	$1.6 \times 10^{-3}$	80	$2.5 \times 10^{-3}$

SMBH mass at  $z \sim 6$ . We refer the reader to Valiante et al. (2016b; and references therein) for a detailed description of the original model.

## 2.1 Dark matter haloes evolution

For a statistical analysis, we reconstruct 10 merger histories of a DM halo of  $M_{\text{halo}} = 10^{13} M_{\odot}$  at  $z_0 = 6.42$ , presumably hosting an SMBH (Willott, McLure & Jarvis 2003; Cubbon et al. 2007). We perform a binary Monte Carlo algorithm to decompose, backwards in time, the massive DM halo into its progressively less massive progenitors, from  $z_0$  back to  $z = 24$ .

At a given redshift  $z$ , the resolution mass of the simulated merger trees, i.e. the minimum mass of a virialized structure, is described as in Valiante et al. (2020):

$$M_{\text{res}}(z) = 10^{-3} M_{\text{halo}} \left( \frac{1+z}{1+z_0} \right)^{\beta}, \quad (1)$$

where  $\beta = -7.5$  (Valiante et al. 2016b), so that  $M_{\text{res}} \sim 10^6 (10^{10}) M_{\odot}$  at  $z = 24 (z = z_0)$ . Lower mass fragments, i.e. unresolved structures with  $M < M_{\text{res}}$ , account for the external medium from which haloes accrete mass, that we refer to as intergalactic medium (IGM). The functional form in equation (2.1) and the redshift-dependent characteristic time interval,  $\Delta t$  (ranging between 0.2 and 2 Myr), are designed to ensure the binarity of the merger tree ( $< 2$  progenitors per halo), to resolve the formation of high- $z$  minihaloes, to reproduce the halo mass function predicted by the extended Press–Schechter formalism (Lacey & Cole 1993) and to contain computational costs.

## 2.2 Star formation and feedback

### 2.2.1 Star formation law

Along a merger tree, each progenitor galaxy can form stars according to the available gas budget,  $M_{\text{gas}}$ . The star formation rate (SFR) is described as

$$\text{SFR} = f_{\text{cool}} M_{\text{gas}} \epsilon / \tau_{\text{dyn}}(z), \quad (2)$$

where  $\tau_{\text{dyn}}(z)$  is the halo dynamical time,  $\epsilon = \epsilon_{\text{quiesc}} + \epsilon_{\text{burst}}$  is the sum of the quiescent and merger-driven starburst efficiencies and is one of the model-free parameters, which have been set to reproduce the observed properties of a proto-typical  $z \sim 6$  quasar (QSO) and its host galaxy (see Table 1 for the complete set of free parameters). We assume stars to form with a constant efficiency  $\epsilon_{\text{quiesc}} = 0.1$  that can be enhanced to  $\epsilon_{\text{quiesc}} + \epsilon_{\text{burst}}$  during galaxy major mergers due to a reduction in the time-scales for star formation from  $\tau_{\text{quiesc}} = \tau_{\text{dyn}} / \epsilon_{\text{quiesc}}$  to  $\tau_{\text{burst}} = \tau_{\text{dyn}} / (\epsilon_{\text{burst}} + \epsilon_{\text{quiesc}})$ . Following Valiante et al. (2011), we assume  $\epsilon_{\text{burst}}$  to be a function of the ratio  $\mu$  between the mass of the less massive halo over the more massive companion and

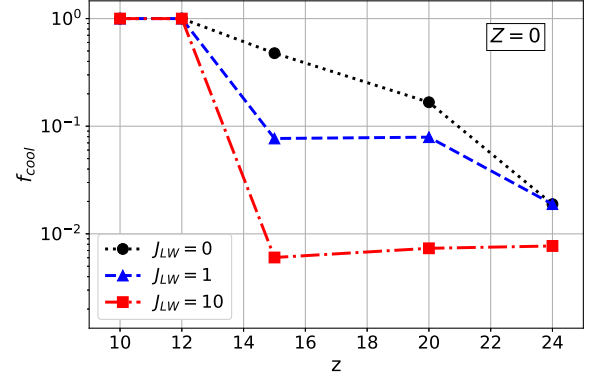


**Figure 1.** The predicted reduced cooling efficiency  $f_{\text{cool}}$  in minihaloes as a function of redshift. The black-, blue-, and red-dashed lines correspond to different values of the LW flux ( $J_{\text{LW}} = 0, 1, 10$ , respectively) illuminating haloes with mass equal to the resolution mass of the simulation,  $M_{\text{vir}} = M_{\text{res}}(z)$ , and with a constant gas metallicity  $Z = 0$ . The resulting cooling efficiency is independent of metallicity for poorly enriched ( $Z \leq 10^{-2} Z_{\odot}$ ) minihaloes.

to be described by a normalized Gaussian distribution:

$$\epsilon_{\text{burst}} = \frac{e^{-(\mu - \mu_{\text{crit}})^2 / 2\sigma_{\text{burst}}^2}}{\sqrt{2\pi}\sigma_{\text{burst}}} \quad (3)$$

with  $\sigma_{\text{burst}} = 0.05$ ,  $\mu_{\text{crit}} = 1$ , and  $\mu > 1/4$ , which defines the threshold for galaxy major mergers. For equal mass mergers ( $\mu = \mu_{\text{crit}}$ ), this leads to a maximum value of  $\epsilon_{\text{burst}} = 8$ , reducing the time-scale for star formation,  $\tau_{\text{burst}} / \tau_{\text{quiesc}} = \epsilon_{\text{quiesc}} / (\epsilon_{\text{quiesc}} + \epsilon_{\text{burst}}) \sim 0.012$ .

Finally, the parameter  $f_{\text{cool}}$  in equation (2) quantifies the reduced cooling efficiency of minihaloes with respect to atomic cooling haloes, which we discuss below.

### 2.2.2 Radiative feedback

In each galaxy, the efficiency of gas cooling and star formation is regulated by radiative feedback. In our model, we account for the effects of both photodissociating and photoheating feedback.

At low metallicity, the gas cooling efficiency in minihaloes relies only on molecular hydrogen, which can be easily dissociated by photons in the LW band. We account for this effect through the parameter  $f_{\text{cool}}$  entering in equation (2). In particular, we set  $f_{\text{cool}} = 1$  in atomic cooling haloes, whereas in minihaloes its value ( $\leq 1$ ) depends on the halo virial temperature,  $T_{\text{vir}}$ , redshift, gas metallicity, and intensity of the illuminating LW flux,  $J_{\text{LW}}$ , expressed in units of  $10^{-21} \text{ erg s}^{-1} \text{ Hz}^{-1} \text{ cm}^{-2} \text{ sr}^{-1}$  (see Valiante et al. 2016b; de Bressan et al. 2017, for details). In Fig. 1, we show the redshift evolution of the reduced cooling efficiency for the least massive haloes [for haloes with  $M_{\text{vir}} = M_{\text{res}}(z)$ ] assuming three different values of the LW irradiating flux,  $J_{\text{LW}} = 0, 1$ , and 10, and a constant gas metallicity equal to  $Z = 0$ . Similar results are found for gas metallicity in the range  $0 \leq Z \leq 10^{-2} Z_{\odot}$ . The figure shows that even when  $J_{\text{LW}} = 0$ ,  $f_{\text{cool}}$  ranges between 0.02 and 1 due to less efficient cooling by molecular hydrogen. At  $z > 12$ ,  $M_{\text{res}}(z)$  corresponds to mini-haloes and  $f_{\text{cool}}$  is very sensitive to the illuminating LW radiation field. At  $z \leq 12$ ,  $M_{\text{res}}(z)$  grows above the halo mass with  $T_{\text{vir}} = 10^4 \text{ K}$  and  $f_{\text{cool}} = 1$  in atomic cooling haloes. When  $J_{\text{LW}} = 100$ ,  $f_{\text{cool}} = 0$  at all redshifts greater than 12 and star formation in mini-haloes is completely suppressed.

Even in atomic cooling haloes star formation can be inhibited as a consequence of the increased gas temperature within photoionized

regions. We assume  $\epsilon = 0$  in equation (2) when the halo virial temperature is below the IGM temperature,  $T_{\text{vir}} < T_{\text{IGM}}$ . The latter is computed as

$$T_{\text{IGM}} = Q_{\text{HII}}(z)T_{\text{reio}} + [1 - Q_{\text{HII}}(z)]T_{\text{gas}}, \quad (4)$$

where  $Q_{\text{HII}}(z)$  is the filling factor of H II regions,  $T_{\text{reio}} = 2 \times 10^4$  K is the post-reionization temperature and  $T_{\text{gas}} = 170$  K  $[(1+z)/100]^2$ . We compute the time evolution of  $Q_{\text{HII}}(z)$  as

$$\frac{dQ_{\text{HII}}}{dt} = f_{\text{esc}}\dot{n}_{\gamma}/n_{\text{H}} - \alpha_{\text{B}} C n_{\text{H}}(1+z)^3 Q_{\text{HII}}, \quad (5)$$

where  $f_{\text{esc}} = 0.1$  is the escape fraction of ionizing photons,  $\dot{n}_{\gamma}$  is the total production rate of ionizing photons per unit volume summed over all the emitting sources,  $n_{\text{H}}$  is the comoving hydrogen number density in the IGM,  $\alpha_{\text{B}} = 2.6 \times 10^{-13}$  cm<sup>3</sup> s<sup>-1</sup> is the hydrogen recombination rate, and  $C = 3$  is the clumping factor (for more details, see Valiante et al. 2016b).

### 2.2.3 Chemical and mechanical feedback

In GQd stars form according to a Larson IMF (Larson 1998)

$$\phi(m_*) \propto m_*^{(\alpha-1)} e^{-m_{\text{ch}}/m_*}, \quad (6)$$

where  $m_*$  is the stellar mass,  $m_{\text{ch}}$  is the characteristic mass, and  $\alpha = -1.35$ . In metal-free/poor ( $Z < Z_{\text{cr}} = 10^{-3.8} Z_{\odot}$ ) environments we adopt an IMF constrained by stellar archaeology data (de Bressan et al. 2014), with Pop III stars forming in the mass range [10–300]  $M_{\odot}$  and  $m_{\text{ch}} = 20 M_{\odot}$ . In addition, when the star formation efficiency is low, we randomly sample the above IMF to predict the stellar mass distribution present in each system (see Valiante et al. 2016b, for details). Once the metallicity increases above the threshold  $Z > Z_{\text{cr}} = 10^{-3.8} Z_{\odot}$ , metal fine-structure line cooling becomes efficient (Omukai et al. 2005) and we assume Pop III stars to form in the range [0.1–100]  $M_{\odot}$  with  $m_{\text{ch}} = 0.35 M_{\odot}$ .

In each galaxy, evolving stars progressively enrich the ISM with metals and dust. Their abundances are computed adopting the grids of stellar yields provided by van den Hoek & Groenewegen (1997) and Zhukovska, Gail & Tieloff (2008) for AGB stars (1–8  $M_{\odot}$ ), Woosley & Weaver (1995) and Bianchi, Schneider & Valiante (2009) for core-collapse SNe (10–40  $M_{\odot}$ ) and Heger & Woosley (2002) and Bianchi et al. (2009) for pair-instability SNe (PISNe; 140–260  $M_{\odot}$ ). For our adopted Pop III IMF, the largest contribution to the metal and dust yields is provided by the most massive stars (see the left-hand panel of fig. 2 in de Bressan et al. 2014), for which the assumption of instantaneous recycling is a good approximation. Hence, Pop III stars are assumed to evolve instantaneously, i.e. their lifetime is the characteristic time interval of the merger tree, while Pop III stellar lifetimes are computed according to the parametric form proposed by Raiteri, Villata & Navarro (1996) and depend on the stellar mass and metallicity. Once injected in the ISM, the abundance of dust grains is computed accounting for grain destruction by SN shocks and grain growth in the dense, cold ISM phase (for additional details, see Valiante et al. 2014).

Finally, SN explosions deposit energy in the ISM, driving a galaxy-scale wind (mechanical feedback),

$$\frac{dM_{\text{ej,SN}}(t)}{dt} = \frac{2E_{\text{SN}}\epsilon_{\text{w,SN}}R_{\text{SN}}(t)}{v_{\text{c}}^2}, \quad (7)$$

that is proportional to the rate of SN explosions,  $R_{\text{SN}}(t)$ , to the average SN explosion energy,  $E_{\text{SN}}$ , and to an efficiency parameter,  $\epsilon_{\text{w,SN}}$ , that accounts for the fact that only a small fraction of the total energy injected by the SNe is in kinetic form and coupled to the gas, while

the rest is dissipated and converted into thermal energy (see e.g. Walch & Naab 2015). The quantity  $R_{\text{SN}}(t)$  depends on the SFR and on the stellar IMF,  $E_{\text{SN}} = 2.7 \times 10^{52}$  erg for Pop III stars and  $1.2 \times 10^{51}$  erg for Pop II/I stars, and  $\epsilon_{\text{w,SN}}$  is a free parameter that we calibrate based on the observations (see Table 1).

### 2.3 BH seeding prescriptions

As introduced in Section 1, seeds expected to form under specific environmental conditions (level of illuminating LW radiation, metal, and dust composition of the ISM). In GQd, such properties are computed consistently with the overall evolution of the galaxy and nuclear black hole populations (Valiante et al. 2016b, 2018a,b).

*Light seeds* form as end-products of Pop III stars, in minihaloes or atomic cooling haloes where gas cooling is dominated by H<sub>2</sub>. This implies that the illuminating LW flux must be subcritical,  $J_{\text{LW}} < J_{\text{cr}}$ , and that metal- and dust-cooling must not operate, hence the metallicity  $Z < Z_{\text{cr}}$  and the gas-to-dust mass ratio  $\mathcal{D} < \mathcal{D}_{\text{cr}}$ . In these conditions, the star formation efficiency is relatively low and only a small number of stars is formed. The mass of the BH remnants depends on the initial mass of the (stochastically sampled) stars (Woosley, Heger & Weaver 2002): stars in the mass ranges [40–140]  $M_{\odot}$  and [260–300]  $M_{\odot}$  directly collapse into a BH with a mass equal to the progenitor mass; in the mass range [140–260]  $M_{\odot}$ , the stars explode as PISN and leave no remnant. Depending on the star formation efficiency, these different mass ranges are unequally sampled and therefore the emerging BH mass distribution is not unique.

We assume that the heaviest among all the formed BHs migrate to the centre by dynamical friction, and we tag this as the nuclear *light seed*. If a halo hosts multiple Pop III star formation episodes, we repeat the random sampling procedure and we assume the heaviest among the new BH population to migrate to the centre and to merge with the previous nuclear BH, generating a new heavier *light seed*.

*Heavy seeds* mediated by the collapse of an SMS require the gas to monolithically collapse with no fragmentation (Omukai et al. 2008). This, in turn, requires the gas to be hosted in atomic cooling haloes that are illuminated by a sufficiently strong LW flux to inhibit H<sub>2</sub> cooling and, similar to *light seeds*, metal and dust cooling must not operate. In this scenario, we plant a *heavy seed* of  $10^5 M_{\odot}$  in atomic cooling haloes where  $J \geq J_{\text{cr}}$ , and  $Z < Z_{\text{cr}}$  and  $\mathcal{D} < \mathcal{D}_{\text{cr}}$ . In addition, we require the halo not to have experienced previous episodes of star formation and to have a sufficiently large reservoir of gas  $M_{\text{gas}} \geq 10^6 M_{\odot}$  (condition required to fuel strong accretion on to the forming SMS).

Following Valiante et al. (2016b), in our reference model (which we call R300) we assume  $J_{\text{cr}} = 300$  (expressed in units of  $10^{-21}$  erg s<sup>-1</sup> Hz<sup>-1</sup> cm<sup>-2</sup> sr<sup>-1</sup>),  $Z_{\text{cr}} = 10^{-3.8} Z_{\odot}$ , and  $\mathcal{D}_{\text{cr}} = 4.4 \times 10^{-9}$  (Schneider et al. 2012).

### 2.4 Black hole growth and feedback

The model GQd follows the mass growth of nuclear black holes through gas accretion and the coalescence with other black holes, starting from a seed population that depends on the environmental conditions as discussed above.

We assume that two nuclear BHs coalesce only in major merger events, i.e. when  $\mu \geq 1/4$ .<sup>1</sup> Although post-merger BH ejection due to

<sup>1</sup>We assume a galaxy merger to occur within the redshift-dependent time-step of the simulation,  $\Delta t$ , which ranges from a fraction to a few Myr.

asymmetric GW emission may have an impact on the SMBH growth, especially at high  $z$  (see e.g. Pezzulli et al. 2016), in this analysis we neglect the gravitational recoil effect in order to compare our results with Valiante et al. (2016b) but focusing on the relative role of all three BH seeds populations for  $z > 6$  SMBHs growth.

In minor halo–halo mergers ( $\mu < 1/4$ ), we instead assume that only the most massive BH will settle in the nuclear region of the newly formed galaxy, where it can start accreting gas. The lighter one is considered as a satellite, wandering in the galaxy outskirts, and we do not follow its subsequent evolution. Such a conservative assumption is independent of the mass ratio of the two BHs involved in the galaxy merger event. However, during wet (gas-rich) minor galaxy mergers (down to 1:10), the satellite BH may grow faster than the primary so that it may orbit towards the centre as well (see e.g. Callegari et al. 2009, 2011; Van Wassenhove et al. 2014; Capelo et al. 2015). We plan to investigate this effect, together with a more refined description of BH dynamics (including gravitational recoil) in future works.

Thus, not all the nuclear BHs present at  $z > 6.4$  will directly contribute to the final SMBH mass, as some of these may be involved in minor halo–halo mergers and become wandering BHs at later times. The real SMBH progenitors are identified by reconstructing the assembly history backwards in time up to the seeds formation epoch.

As in Valiante et al. (2011, 2014) and Valiante, Schneider & Volonteri (2016a), BH mass growth by gas accretion proceeds at a rate given by  $\dot{M}_{\text{acc}} = \min[\dot{M}_{\text{Edd}}, \dot{M}_{\text{BHL}}]$ , where  $\dot{M}_{\text{Edd}}$  is the Eddington rate,

$$\dot{M}_{\text{Edd}} = \frac{4\pi G M_{\text{BH}} m_{\text{p}}}{\epsilon_{\text{r}} \sigma_{\text{T}} c}, \quad (8)$$

and  $\dot{M}_{\text{BHL}}$  is the Bondi–Hoyle–Lyttleton accretion rate (Hoyle & Lyttleton 1939; Bondi & Hoyle 1944; Bondi 1952),

$$\dot{M}_{\text{BHL}} = \frac{4\pi \alpha_{\text{BH}} G^2 M_{\text{BH}}^2 \rho_{\text{gas}}(r_{\text{A}})}{c_{\text{s}}^3}. \quad (9)$$

In the above equations,  $m_{\text{p}}$  is the proton mass,  $\epsilon_{\text{r}} = 0.1$  is the radiative efficiency,  $\sigma_{\text{T}}$  is the Thomson scattering cross-section,  $G$  is the gravitational constant,  $c$  is the speed of light,  $\rho_{\text{gas}}(r_{\text{A}})$  is the gas density<sup>2</sup> at the radius of gravitational influence of the BH (also called Bondi radius,  $r_{\text{A}} = 2GM_{\text{BH}}/c_{\text{s}}^2$ ), and  $c_{\text{s}}$  is the sound speed. The dimensionless parameter  $\alpha_{\text{BH}}$  is usually introduced in numerical simulations to compensate for the lack of resolution that heavily underestimates the BHL accretion rate (Springel, Di Matteo & Hernquist 2005) and is a free parameter of the model (see Table 1).

Numerical simulations show that feedback due to SNe appears crucial in regulating BH growth in low-mass galaxies (Dubois et al. 2015) and therefore affects the BH mass distribution after the formation epoch of BH seeds (Habouzit et al. 2016a). Our model describes the total outflow rate from a galaxy as the sum of the active galactic nucleus (AGN) and SN contributions,

$$\frac{dM_{\text{ej}}(t)}{dt} = \frac{dM_{\text{ej,AGN}}}{dt} + \frac{dM_{\text{ej,SN}}}{dt}, \quad (10)$$

<sup>2</sup>Following Valiante et al. (2011), we assume the gas to follow an isothermal density distribution with a flat core. The core radius is assumed to be 0.012 times the DM halo virial radius and the profile is normalized such that at each time the total gas mass predicted by the model is enclosed within the virial radius. We refer the reader to Valiante et al. (2011) for additional details.

and the energy-driven AGN gas outflow (wind) is described as

$$\frac{dM_{\text{ej,AGN}}}{dt} = 2\epsilon_{\text{w,AGN}} \epsilon_{\text{r}} \dot{M}_{\text{accr}} \left(\frac{c}{v_{\text{e}}}\right)^2, \quad (11)$$

where  $\epsilon_{\text{w,AGN}}$  is the wind efficiency. AGN winds are assumed to be in action when the accretion rate exceeds  $10^{-2} \dot{M}_{\text{Edd}}$  ( $dM_{\text{ej,AGN}}/dt = 0$  otherwise). Even with our simplified treatment of AGN and SN feedback, BHs often starve due to gas evacuation, particularly in the small haloes at high  $z$  that are characterized by small escape velocities. In this regime, the BH duty cycle is set by halo mass growth via mergers, which provide additional gas supply to the nuclear regions, restarting a new cycle of star formation and BH growth.

### 3 NEW FEATURES OF THE MODEL

In this section, we describe the new physically motivated prescriptions implemented in the model to investigate the occurrence of *light*, *heavy*, and *medium-weight* seeds in a cosmological context and their relative importance/role in the formation of  $z > 6$  SMBHs.

#### 3.1 Medium-weight seeds

As we have seen in Section 2.3, a necessary condition for the monolithic collapse is to avoid fragmentation. When dust-driven cooling is effective, which is when  $\mathcal{D} \geq \mathcal{D}_{\text{cr}}$  (Schneider et al. 2012), fragmentation occurs at very high densities and in a very compact region, potentially leading to the formation of a dense stellar cluster (Clark, Glover & Klessen 2008; Omukai et al. 2008).

The question is then to understand what is the final fate of this system. During their lifetime, collisional stellar systems evolve as a result of dynamical interactions. In an equal-mass system, the central cluster core initially contracts as the system attempts to reach a state of thermal equilibrium: energy conservation leads to a decrease in the core radius as evaporation of the less bound stars proceeds. As a result, the central density increases and the central relaxation time decreases. The core then decouples thermally from the outer region of the cluster. Core collapse then speeds up as it is driven by energy transfer from the central denser region (Gürkan, Freitag & Rasio 2004; Reinoso et al. 2018; Reinoso et al. 2019). This phenomenon is greatly enhanced in multimass systems like realistic star clusters. In this case, the gravothermal collapse happens on a shorter time-scale as dynamical friction causes the more massive than  $m_{\ast}$  stars to segregate in the center on a time-scale  $t_{\text{df}} = (\langle m \rangle / m_{\ast}) t_{\text{rh}}$ , where  $t_{\text{rh}}$  is the half-mass relaxation time-scale, and  $\langle m \rangle$  is the mean stellar mass in the cluster (Portegies Zwart & McMillan 2002; Devecchi & Volonteri 2009). If mass segregation sets in before the more massive stars evolve out of the main sequence ( $\sim 3$  Myr), then a subsystem decoupled from the rest of the cluster can form, where star–star collisions can take place in a runaway fashion, ultimately leading to the growth of a very massive star (VMS). The upper limit on the duration of the process ( $\sim 3$  Myr) is set by the requirement to avoid the explosion of the SNe, which would sweep away the system (Sakurai et al. 2017).

If a VMS forms above  $260 M_{\odot}$ , it would directly collapse into a BH of comparable mass. In addition, the BH can still gain mass by accretion of stars and from the surrounding gas (Devecchi & Volonteri 2009). Since mass-loss due to winds is significantly reduced in metal-poor stars, the growth of a VMS should be more efficient at low metallicity and the resulting BH mass can be as high as  $10^3 M_{\odot}$  (Devecchi & Volonteri 2009; Volonteri 2010).

Hence, in GQd we assume that a *medium-weight seed* forms in atomic cooling haloes ( $T_{\text{vir}} \geq 10^4$  K) where the gas is illuminated by

**Table 2.** The environmental conditions adopted to plant the three families of seeds in the GQD reference (R) model and in the supercompetitive accretion (SCA) variant (see Sections 2.3 and 3). For each of these models, two values of  $J_{\text{cr}}$  have been explored: 300 and 1000.

R model	$Z/Z_{\odot}$	$\mathcal{D}$	$J_{\text{LW}}$	$M_{\text{gas}}$
Light	$<10^{-3.8}$	$<4.4 \times 10^{-9}$	$<J_{\text{cr}}$	$>0$
Medium	$<10^{-3.8}$	$\geq 4.4 \times 10^{-9}$	$\geq J_{\text{cr}}$	$>10^6 M_{\odot}$
Heavy	$<10^{-3.8}$	$<4.4 \times 10^{-9}$	$\geq J_{\text{cr}}$	$>10^6 M_{\odot}$
SCA model	$Z/Z_{\odot}$	$\mathcal{D}$	$J_{\text{LW}}$	$M_{\text{gas}}$
Light	$<10^{-3.8}$	$<4.4 \times 10^{-9}$	$<J_{\text{cr}}$	$>0$
Medium	$[10^{-3.5} - 10^{-2.5}]$	all	$\geq J_{\text{cr}}$	$>10^6 M_{\odot}$
Heavy	$<10^{-3.5}$	all	$\geq J_{\text{cr}}$	$>10^6 M_{\odot}$

a LW flux with  $J_{\text{LW}} \geq J_{\text{cr}}$ , the metal content of the ISM is subcritical,  $Z < Z_{\text{cr}}$ , but the dust content is supercritical,  $\mathcal{D} \geq \mathcal{D}_{\text{cr}}$ , so that dust cooling can lead to the formation of a dense star cluster. In addition, we require the halo to have a sufficiently large reservoir of gas,  $M_{\text{gas}} \geq 10^6 M_{\odot}$ , to form a dense and compact star cluster and we assume its final fate to be the formation of a medium-weight seed with a mass of  $10^3 M_{\odot}$ .

The environmental conditions required to form *light*, *medium-weight*, and *heavy* seeds in GQD are summarized in Table 2. In Section 4, we discuss the effects of varying the adopted critical threshold for the LW flux to suppress  $\text{H}_2$  formation. In addition, following Chon & Omukai (2020), we also consider a variant of the reference model where we account for SCA, which we illustrate below.

### 3.2 The supercompetitive accretion model

In a recent work, Chon & Omukai (2020; see also Tagawa et al. 2020) used a suite of hydrodynamical simulations to investigate the outcome of star formation in slightly metal-enriched gas clouds illuminated by a very strong UV field. The initial conditions were set by extracting – from a cosmological simulation – one halo that was shown to lead to the formation of a heavy seed when the gas was metal-free (Chon et al. 2018). As expected from previous semi-analytical models (Omukai et al. 2008), dust-cooling becomes important when  $Z \geq 5 \times 10^{-6} Z_{\odot}$  and multiple (about 600) low-mass fragments form in a relatively compact region with size smaller than 100 au. On larger scales, however, where dust cooling is not effective, the structure of the cloud is very similar to the primordial case: as a result of the high gas temperatures, matter continues to flow into the central regions, preferentially feeding the primary star (defined as the first protostar that forms). In  $10^4$  yr the primary star becomes supermassive, with a mass comparable to the one found in the primordial case. Interestingly, a similar evolution is found for initial metallicities up to  $Z = 10^{-4} Z_{\odot}$ , although the initial number of low-mass protostars formed as a result of dust-cooling increases with  $Z$  (about 4000 stars are formed when  $Z = 10^{-4} Z_{\odot}$ ). When the metallicity becomes  $Z = 10^{-3} Z_{\odot}$  (the maximum metallicity considered in their analysis), Chon & Omukai (2020) found that metal fine-structure line cooling starts to be effective on larger scales (when the central gas density is  $n \geq 10^4 \text{ cm}^{-3}$ ), and the associated decrease in the gas temperature leads to a suppression of the gas accretion rate by almost two orders of magnitude. As a result, the primary star mass grows only up to  $350 M_{\odot}$ . It is important to stress, however, that some of the secondary protostars merge with the primary stars. Although the fraction of mass acquired through mergers is subdominant when  $Z < 10^{-4} Z_{\odot}$ , mergers contribute to

more than 50 per cent of the final primary mass when  $Z = 10^{-3} Z_{\odot}$ . Since the total stellar mass formed in this highest metallicity run is  $\geq 10^3 M_{\odot}$ , this may imply that the resulting primary star may grow further if the evolution were followed for more than the  $10^4$  yr allowed by the simulation.

Hence, in this SCA model, SMSs leading to heavy BH seeds may continue to form at higher metallicities than assumed in our reference model. To investigate how this alternative scenario would modify the relative importance of the different BH seed populations, we run additional simulations where the conditions to form medium-weight and heavy seeds are set as follows: atomic cooling haloes illuminated by a supercritical LW flux host the formation of heavy seeds as long as  $Z < 10^{-3.5} Z_{\odot}$ , and of medium-weight seeds when  $10^{-3.5} Z_{\odot} \leq Z < 10^{-2.5} Z_{\odot}$  independent of their dust-to-gas mass ratio. Conversely, the transition from Pop III to Pop II stars is still assumed to occur when  $Z \geq Z_{\text{cr}} = 10^{-3.8} Z_{\odot}$  and  $\mathcal{D} > 4.4 \times 10^{-9}$  so that this model variant does not directly affect the conditions to form light seeds (see Table 2).

### 3.3 Inhomogeneous feedback

In the GQD model, metals and dust returned to the ISM through SN explosions and AGB stellar winds are assumed to instantaneously mix in the ISM. In addition, SN- and AGN-driven outflows described in Section 2 have a metal and dust composition that reflect the conditions at the outflow launching site. Once ejected in the IGM, we assume metals and dust to uniformly mix with the surrounding gas. This is the pre-enriched medium that will be accreted on to newly virialized DM haloes, and out of which new stellar and/or BH seeds will form.

In Valiante et al. (2016b), the formation rate of *light* and *heavy* seeds was analysed by applying the same conditions described in Section 2.3 and summarized in Table 2 for the reference model. We found that, under the hypothesis of uniform metal/dust mixing and uniform LW background, the redshift window where haloes satisfied the conditions for *heavy seeds* formation was extremely narrow, and only a few *heavy seeds* (between 3 and 30, depending on the simulation) were able to form. This number, however, was enough to trigger the Eddington-limited growth to an SMBH by  $z \sim 6$  (Valiante et al. 2016b).

However, metal (and dust) enrichment is known to be a highly inhomogeneous process, particularly at high redshift. Cosmological hydrodynamic simulations (Tornatore, Ferrara & Schneider 2007; Maio et al. 2011; Wise et al. 2012; Johnson, Dalla Vecchia & Khochfar 2013; Muratov et al. 2013; Pallottini et al. 2015; Xu et al. 2016; Jaacks et al. 2018; Graziani et al. 2019; Sarmiento, Scannapieco & Côté 2019) supported by observations (Robert et al. 2019; Vanzella et al. 2020) show that metals ejected in the ISM by SNe and AGB stars propagate from higher density peaks to lower density regions, allowing the co-existence of pristine and metal-enriched objects in the pre-reionization epoch.

Similarly, although the intensity of the LW background produced by stellar sources and accreting black holes increases very rapidly in the biased region where the bright quasar and its host galaxy are assembling (see fig. 5 of Valiante et al. 2016b), local fluctuations of the LW intensity from nearby sources can significantly exceed the background level, suppressing  $\text{H}_2$  cooling and aiding to win the competition between LW radiation and metal winds in *heavy seeds* hosts (Ahn et al. 2009; Dijkstra et al. 2014; Regan et al. 2014; Inayoshi & Tanaka 2015; Habouzit et al. 2016a; Agarwal et al. 2017; Maio et al. 2019; Mayer & Bonoli 2019; Lupi et al. 2021).

Since we do not have any information on the spatial distribution of DM haloes in the simulated volume, or on the spatial distribution of metal-enriched bubbles, we have implemented in GQD a statistical description of inhomogeneous chemical and radiative feedback that we present below.

### 3.3.1 Inhomogeneous metal and dust enrichment

Following Dijkstra et al. (2014) and Salvadori et al. (2014), at each redshift we compute the volume filling factor of the N-enriched regions as

$$Q(z) = \sum_{i=1}^N \frac{V_i}{V_{\text{sim}}} = \sum_{i=1}^N \frac{4/3 \pi R_i^3}{V_{\text{sim}}}, \quad (12)$$

where  $\sum_{i=1}^N V_i$  is the volume filled by SN-driven, metal-enriched bubbles with radius  $R_i$  and  $V_{\text{sim}} = 50 \text{ Mpc}^3 (1+z)^{-3}$  is the proper volume of the simulation, estimated at the turnaround radius. At a given time (redshift), the radius of the  $i$ th expanding bubble polluted by metals can be approximated by the self-similar Sedov–Taylor blastwave solution (Madau, Ferrara & Rees 2001; Dijkstra et al. 2014):

$$R_i(t) = \xi_0 \left[ \frac{E_{\text{SN}} N_{\text{SN},i}}{\rho_{\text{gas}}(z_i)} \right]^{1/5} t^{2/5}, \quad (13)$$

where  $\xi_0 = 1.17$ ,  $E_{\text{SN}} N_{\text{SN},i}$  is the total SN explosion energy in the  $i$ th halo [ $E_{\text{SN}}$  is the averaged energy per SN, as in equation (7), and  $N_{\text{SN}}$  is the number of SNe]<sup>3</sup>  $\rho_{\text{gas}}$  is the gas density and  $t = t(z) - t(z_i)$  is the interval between the current time  $z$  and the redshift  $z_i$  at which the SN-driven outflow was launched. When the bubble is within the halo virial radius,  $R_i < R_{\text{vir},i}$ ,  $\rho_{\text{gas}}$  is the mean gas density of the  $i$ th halo at the moment of the SNe explosion. As the bubble expands beyond the halo virial radius into the IGM,  $R_i > R_{\text{vir},i}$ , we compute the gas density<sup>4</sup> as  $\rho_{\text{gas}}(z) = \Omega_b \rho_{\text{cr}} (1+z)^3$ .

At a given time (redshift) we define the mean metallicity,  $Z_q$ , and dust-to-gas mass ratio,  $\mathcal{D}_q$  of the enriched regions as

$$Z_q(t) = \frac{M_{\text{met},\text{ej}}^{\text{tot}}(t)}{M_{\text{ej}}^{\text{tot}}(t) + [1 - f_c(t)] \sum_{i=1}^N \Omega_b \rho_{\text{cr}} (1+z)^3 V_i}, \quad (14)$$

and

$$\mathcal{D}_q(t) = \frac{M_{\text{dust},\text{ej}}^{\text{tot}}(t)}{M_{\text{ej}}^{\text{tot}}(t) + [1 - f_c(t)] \sum_{i=1}^N \Omega_b \rho_{\text{cr}} (1+z)^3 V_i}. \quad (15)$$

where  $M_{\text{ej}}^{\text{tot}}(t)$ ,  $M_{\text{met},\text{ej}}^{\text{tot}}(t)$ , and  $M_{\text{dust},\text{ej}}^{\text{tot}}(t)$  are the total masses of gas, metals, and dust, respectively, that have been ejected out of the haloes in the IGM,  $[1 - f_c(t)] \sum_{i=1}^N \Omega_b \rho_{\text{cr}} (1+z)^3 V_i$  is the IGM gas mass enclosed in the volume covered by the bubbles expanding outside the haloes (the summation runs on all haloes for which the condition  $R_i > R_{\text{vir},i}$  is satisfied), and  $f_c(t)$  is the time-dependent fraction of mass collapsed into haloes. The amount of gas ejected out of a single halo as a consequence of mechanical feedback,  $M_{\text{ej}}$ , is computed as described in Section 2. The corresponding mass of ejected metals

<sup>3</sup>During the Sedov–Taylor expansion phase the energy is conserved and not radiated away. Hence, in equation (13), we consider all the energy (kinetic and thermal) injected by each SN.

<sup>4</sup>We note that this may lead to an unphysical jump in the gas density as the bubble reaches the virial radius. However, adopting a smoother transition, such as the one predicted by Madau et al. (2001), delays the time evolution of the shell radius for a very small time interval and provides a negligible correction to the time evolution of the filling factor.

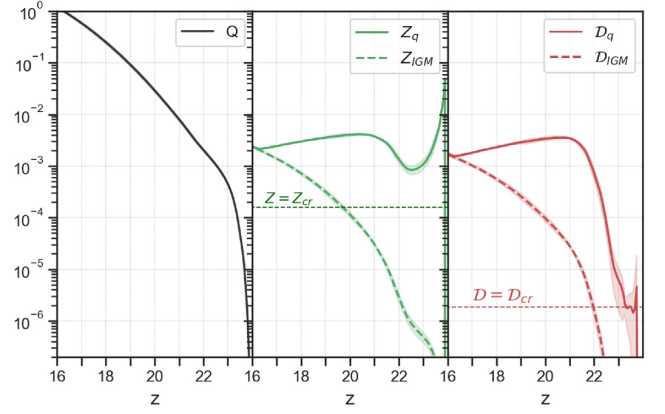


**Figure 2.** Left-hand panel: evolution of the filling factor of enriched regions (the black line) as a function of redshift. Central panel: mean metallicity of the IGM (the green-dashed line) and of the enriched regions (the green solid line) expressed in solar units, with  $Z_{\odot} = 0.02$ . Right-hand panel: mean dust-to-gas ratio of the IGM (the red-dashed line) and of the enriched regions (the red solid line) normalized to the Galactic value,  $\mathcal{D}_{\text{MW}} = 0.006$ . The lines are mean values over 10 realizations of the reference model, with  $1\sigma$  error bars (the light-shaded areas). The horizontal dashed lines in the central and right-hand panels are the critical values for metallicity ( $Z_{\text{cr}}$ ) and dust to gas ratio ( $\mathcal{D}_{\text{cr}}$ ) adopted in the reference model.

and dust are computed as  $M_{\text{met},\text{ej}} = Z_{\text{ISM}} M_{\text{ej}}$  and  $M_{\text{dust},\text{ej}} = \mathcal{D}_{\text{ISM}} M_{\text{ej}}$ , where  $Z_{\text{ISM}}$  and  $\mathcal{D}_{\text{ISM}}$  are the metallicity and dust-to-gas ratio of the ISM, respectively (Valiante et al. 2011, 2014).

At each redshift, we assume that the  $i$ th halo has a probability  $P_i(z) \in [0, 1]$ , randomly extracted from a uniform distribution, to be located within a region of the IGM that has been (already) enriched by SN explosions (i.e. regions occupied by expanding bubbles). We then use the volume filling factor,  $Q(z)$ , to assign haloes to the unpolluted or to the enriched volume: if  $P_i(z) > Q(z)$ , the halo resides in the unpolluted volume  $[1 - Q(z)] V_{\text{sim}}$ , where it accretes gas of primordial composition; if  $P_i(z) \leq Q(z)$ , the halo is instead associated to enriched regions, within the volume  $Q(z) V_{\text{sim}}$ , and accretes polluted gas from the IGM.<sup>5</sup> At each given time,  $Z_q$  and  $\mathcal{D}_q$  define the abundance of metals and dust in the (infalling) material, respectively, accreted by haloes forming/evolving in enriched regions, as described above. Fig. 2 shows the redshift evolution of the filling factor ( $Q$ , left-hand panel), metallicity ( $Z_q$ , central panel), and dust-to-gas mass ratio ( $\mathcal{D}_q$ , right-hand panel) of enriched regions predicted by the reference model (see Section 4). While  $Q$  monotonically increases with cosmic time, reaching the value  $Q = 1$  at  $z \sim 16$ , the redshift evolution of  $Z_q$  and  $\mathcal{D}_q$  is not monotonic and depends on the metal and dust yields of the dominant SN population, on their energies, and on the mass of gas swept by the expanding bubbles. At early times, when the SFR is dominated by Pop III stars, the bubbles are still relatively small ( $Q < 1$ ) and there is a very rapid increase in both  $Z_q$  and  $\mathcal{D}_q$ , implying that the few enriched regions are very metal and dust rich. As the bubbles expand, progressively enclosing a larger IGM gas mass,  $Z_q$  and  $\mathcal{D}_q$  decrease. When the SFR starts to be dominated by Pop II stars, at  $z \lesssim 23$ ,  $Z_q$  and  $\mathcal{D}_q$  increase again but then smoothly decline until, at  $z \sim 16$ , when  $Q \sim 1$ , the volume is homogeneously enriched and their values converge to the mean IGM metallicity,  $Z_{\text{IGM}}$ , and dust-to-gas mass ratio,  $\mathcal{D}_{\text{IGM}}$  (shown in Fig. 2 as the dashed lines). The two

<sup>5</sup>Note that, in the limit  $Q(z) \rightarrow 1$ , the IGM is completely filled by metal-enriched bubbles and the enriched volume converges to the total volume of the simulation:  $\sum_{i=1}^N V_i \rightarrow V_{\text{sim}}$ .

horizontal lines in Fig. 2 represent the adopted critical metallicity and dust-to-gas ratio in the reference model (see Table 2). The figure shows that the condition  $Z_{\text{IGM}} \sim Z_{\text{cr}}$  ( $\mathcal{D}_{\text{IGM}} \sim \mathcal{D}_{\text{cr}}$ ) is met already at  $z \sim 20$  ( $z \sim 22$ ). These are the redshifts below which BH seeds can no longer form in models where the IGM is assumed to be uniformly enriched. However, at these cosmic epochs, we predict the filling factor to be still very small ( $Q \sim 10^{-2}$ ) and metal enrichment to be highly inhomogeneous. As a consequence, BH seeds can continue to form down to  $z \sim 16$ , when the volume has been completely filled by metal-enriched bubbles ( $Q = 1$ ). Hence, inhomogeneous enrichment extends the redshift range where BH seeds may potentially form from  $z \sim 20$  to  $z \sim 16$ .

As a final remark, we notice that the above model of inhomogeneous enrichment assumes that the individual enriched bubbles do not overlap. This neglects the effects of clustering, which are likely to be significant for high-redshift star-forming galaxies and may lead to a  $\sim 70$  per cent reduction of  $Q$  at  $z < 17$ , assuming that the enrichment is mostly driven by  $10^6$ – $10^7 M_{\odot}$  haloes.<sup>6</sup> The effects of this reduction would be to extend the epoch of BH seed formation to lower redshift and to favour the formation of heavy BH seeds, which preferentially form in metal-free, atomic-cooling haloes illuminated by a supercritical LW flux, at the expenses of medium-weight BH seeds (see Section 2.3). However, this does not significantly affect the resulting evolution of the SMBH mass (see Section 2.4).

### 3.3.2 Inhomogeneous $J_{\text{LW}}$ flux

Inhomogeneities in the LW flux and their relation with potential sites for heavy BH seeds formation have been investigated for many years (Dijkstra et al. 2008; Ahn et al. 2009; Agarwal et al. 2012; Dijkstra et al. 2014; Inayoshi & Tanaka 2015). In fact, in the redshift range where BH seeds are expected to form, the mean LW background is significantly smaller than the required critical value above which  $\text{H}_2$  cooling in atomic cooling haloes is suppressed, unless the region under investigation is particularly overdense (Valiante et al. 2016a, b). Hence, heavy seeds form when their potential host halo is illuminated by a supercritical  $J_{\text{LW}}$  from a nearby galaxy (Visbal, Haiman & Bryan 2014; Habouzit et al. 2016b; Maio et al. 2019; Regan et al. 2019), whose distance must not be too close in order to avoid gas stripping or tidal distortions, which would prevent the formation of the SMS (Chon et al. 2016).

This motivates the importance of considering the non-linear spatial distribution of the UV emitting sources around a certain atomic cooling halo,  $M_1$ , candidate to host a heavy or medium-weight seed. In other words, the proximity of  $M_1$  to a star-forming halo can easily help the halo to meet the condition that  $J_{\text{LW}} \geq J_{\text{cr}}$ .

To establish the distance between  $M_1$  and a UV source, we start by considering the probability to find another halo at distance  $r$ . Following Inayoshi & Tanaka (2015), the differential probability distribution of finding a halo with mass  $M_2 \pm dM/2$  at a distance  $r \pm$

$dr$  from  $M_1$  is given by

$$\frac{d^2 P(M_1, M_2, z, r)}{dM dr} = 4\pi r^2 (1+z)^3 \times [1 + \xi(M_1, M_2, z, r)] \frac{dn}{dM}, \quad (16)$$

where  $dn/dM$  is the comoving number density of  $M_2$  haloes at redshift  $z$  and  $\xi$  is the non-linear bias (Iliev et al. 2003).

At each redshift of the merger tree, we identify – among all simulated haloes – those candidate to host a BH seed (see Section 2.3 and Table 2),  $M_1$ . For each of these, we consider  $N_r$  spherical shells centered on  $M_1$ , with radii  $r_i$  varying from  $R_{\text{min}} = 10^{-3}$  Mpc to  $R_{\text{max}} = (3V_{\text{sim}}/4\pi)^{1/3}$  Mpc. We then randomly sample the cumulative probability to find, among all possible star-forming haloes  $N_s$ , a source  $j$  at distance  $r_i$ , and we compute the LW intensity that it emits due to star formation,  $I_{\text{stars}}^j$  and BH accretion  $I_{\text{AGN}}^j$ . Finally, we sum all the contributions to compute the total LW flux irradiating each  $M_1$ :

$$J_{\text{LW}} = \sum_{j=1}^{N_s} \sum_{i=1}^{N_r} \frac{(I_{\text{stars},i}^j + I_{\text{AGN},i}^j)}{4\pi r_i^2}. \quad (17)$$

For this study, we follow Iliev et al. (2003) and adopt  $N_r = 300$ .  $I_{\text{stars}}^j$  is computed using the mass (or age) and metallicity-dependent emissivities by Schaerer (2002; for Pop III stars) and Bruzual & Charlot (2003; for Pop II/I stars), while  $I_{\text{AGN}}^j$  is obtained from a standard multitemperature disc model with the addition of a non-thermal power-law component at high energies ( $\propto \nu^{-2}$ ; Shakura 1973; Sazonov, Ostriker & Sunyaev 2004).

## 4 RESULTS

In this section, we start by illustrating the results of the reference model, R300, where we adopt a critical value for the LW flux of  $J_{\text{cr}} = 300$ . We first present the properties of BH seeds formation environments, such as the intensity of the illuminating LW radiation,  $J_{\text{LW}}$ , the metallicity, and the dust-to-gas mass ratio. Then, we quantify the relative contribution of different seed populations to the mass growth history of the final SMBH. We finally explore the implications of changing the value of  $J_{\text{cr}}$  and how the growth history of the SMBH is modified when the SCA model is adopted.

### 4.1 Mean and local LW flux

In Fig. 3, we show the predicted evolution of the mean LW background as a function of redshift (the blue lines) in 10 independent simulations of R300. It is important to stress that this quantifies the LW background in our simulated volume that represents a very biased region that will form a massive halo at  $z = 6.4$ . This is why the solid lines reach values that are larger than the cosmic averages typically found in other studies (see, for instance, fig. 6 in Ahn et al. 2009 or fig. 3 in Dijkstra et al. 2014 where their mean LW background at  $z > 10$  is found to be in the range  $\sim 0.1$ – $10$ ). Since the mean LW background is roughly proportional to the stellar mass density (see equations 12 and 13 in Agarwal et al. 2012), a larger background is to be expected in the highly biased region that will assemble a  $10^{13} M_{\odot}$  halo at  $z = 6.4$ . Indeed, Petri, Ferrara & Salvaterra (2012) find comparably large values when they simulate the assembly of a  $10^{12} M_{\odot}$  halo at  $z \sim 6$  (see their fig. 5).

Conversely, our predicted local fluctuations in the LW field are very consistent with previous findings (see, for example, fig. 3 of Agarwal et al. 2012 or the colour map in fig. 1 of Dijkstra et al. 2014). These are shown with the grey points in Fig. 3, which represent

<sup>6</sup>The average comoving distance between  $10^6$  and  $10^7 M_{\odot}$  haloes at  $z = 10$ – $20$  ranges between  $\langle d \rangle \sim 0.13$  and  $\sim 1.1$  Mpc. The excess probability of finding two haloes with mass  $M = 10^6 M_{\odot}$  ( $10^7 M_{\odot}$ ) separated by a comoving distance  $\langle d \rangle$  at  $10 < z < 20$  can be estimated to range between 1 and 3 (see e.g. fig. 2 in Iliev et al. 2003). Assuming that within  $\langle d \rangle$  we find three times more systems than if these were uniformly distributed, and that their individual metal-enriched bubbles overlap, our estimated filling factor should be reduced by  $\sim 70$  per cent to account for this clustering effect.

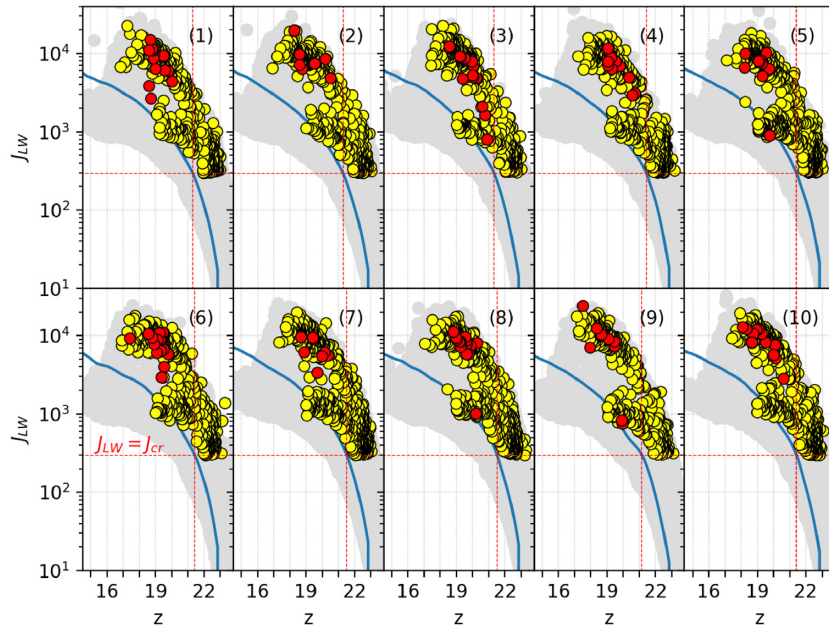


**Figure 3.** The intensity of the LW radiation (in units of  $10^{-21}$  erg s $^{-1}$  Hz $^{-1}$  cm $^{-2}$  sr $^{-1}$ ) as a function of  $z$  for 10 different simulations of model R300. Each grey point represents a single halo, and we have highlighted in red and yellow the formation sites of heavy and medium-weight seeds, respectively. The solid blue line is the mean LW background and the red-dotted lines identify the redshift at which the mean LW background exceeds  $J_{\text{cr}} = 300$ .

the (local) intensity of LW radiation illuminating individual haloes. Among these, we have marked in red (yellow) the formation sites of heavy (medium-weight) seeds. The red-dotted lines identify the redshift at which the mean LW background exceeds the critical value  $J_{\text{cr}} = 300$ . In all simulations, this condition is met at  $z \sim 21$ . While medium-weight seeds can form above this redshift, we find that there are large fluctuations around the mean LW background and in most cases heavy and medium-weight seeds form in environments where  $J_{\text{LW}} > 10^3$ , largely exceeding our adopted value for  $J_{\text{cr}}$ .

#### 4.2 Mean and local metal enrichment

In Fig. 4, we report the ISM metallicity and dust-to-gas mass ratios of individual galaxies extracted from a single simulation (simulation 10 shown in the bottom right-hand panel of Fig. 3) from the onset of chemical enrichment down to the redshift at which the filling factor of enriched regions,  $Q$ , is equal to 1 ( $z \geq 16$ ). We follow the same colour code adopted in Fig. 3, and we mark in red and yellow systems hosting heavy and medium-weight BH seeds, respectively. In addition, we also show the formation sites of light BH seeds, marking in the cyan and blue systems hosted, respectively, in minihaloes and atomic cooling haloes. The solid black line indicates the mean values of the IGM, which shows a monotonic increase of  $D_{\text{IGM}}$  with  $Z_{\text{IGM}}$ .<sup>7</sup> As expected from Fig. 2, when  $Q < 1$ , galaxies located within the already enriched regions have a metallicity and dust-to-gas mass ratio that largely exceed the mean IGM value (and above the critical metallicity and dust-to-gas mass ratio thresholds) populating the upper right end of Fig. 4, together with their lower redshift and metal/dust-rich descendants. On the other hand, unpolluted regions at  $z > 16$  host metal/dust-free ( $Z = D = 0$ ) galaxies that do not appear

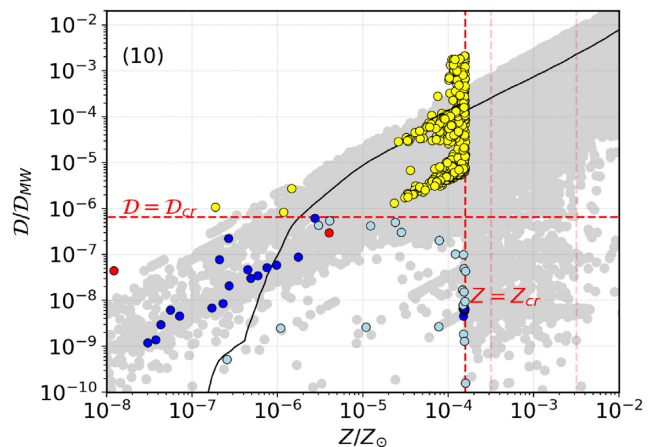


**Figure 4.** The ISM dust-to-gas mass ratio and metallicity of all the star-forming galaxies in simulation (10) at  $z \geq 16$ . Each grey point represents a single halo and – similar to Fig. 3 – we have marked in red and yellow the formation sites of heavy and medium-weight BH seeds. We note that the majority of heavy seeds form in pristine galaxies that are not accounted for in this plane. The cyan and blue points indicate, respectively, non-pristine minihaloes and atomic-cooling haloes where light seeds form. The black solid line represents the mean values of the IGM. The red-dashed lines are the critical dust-to-gas ratio and metallicity thresholds adopted in the reference model. For comparison, the two thin vertical lines show the critical metallicity thresholds adopted in the SCA model (see Fig. 8 and Table 2).

in the figure. This is why the density of grey points is significantly smaller in the bottom left part of the plane.

The two red-dashed lines mark the critical values for  $Z_{\text{cr}}$  and  $D_{\text{cr}}$  adopted in the reference model. These divide the plane in four separate regions: the bottom left part contains the most pristine environments, where only light and heavy BH seeds form. We note that the number of red points is significantly smaller than Fig. 3 (see

<sup>7</sup>We point out that  $D$  and  $Z$  are not always proportional because of dust reprocessing in the ISM due to SN dust destruction and grain growth (see Section 3.3).

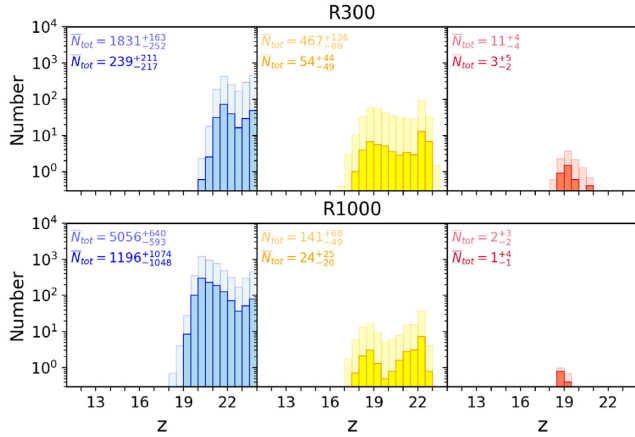


**Figure 5.** Distribution of formation redshifts of light, medium-weight, and heavy BH seeds (from left to right). The histograms indicate the mean values averaged over 10 different simulations. The histograms in lighter colours show the global BH seed population, whereas the histograms in heavier colours illustrate the true progenitors of the final SMBH at  $z = 6.4$  (see text). In each panel, we also indicate the total number of seeds formed, on average, in the corresponding population. The errors indicate the difference with the maximum and minimum values for each family over 10 simulations. We compare the results for the same reference set of parameters, assuming  $J_{\text{cr}} = 300$  (model R300, top panels) and  $J_{\text{cr}} = 1000$  (model R1000, bottom panels).

the bottom right-hand panel). In fact, most of the heavy BH seeds form in pristine haloes, which are not visible in Fig. 4.

A similar consideration applies to light BH seeds, a large fraction of which form when  $Z = \mathcal{D} = 0$ . In the top left region only medium-weight seeds can form, in the subsample of haloes that are illuminated by a supercritical  $J_{\text{LW}}$  and that contain a sufficiently large gas mass ( $\geq 10^6 M_{\odot}$ ). The latter condition preferentially selects systems along diagonal lines on this plane. The highest density of galaxies appears to the right of the vertical line representing  $Z = Z_{\text{cr}}$ , where Pop III stars are assumed to form by metal and dust-driven fragmentation. Indeed, their parent star-forming clouds are either initially enriched above  $\mathcal{D}_{\text{cr}}$  (top right region) or they reach this condition during cloud collapse through grain growth (Chiaki et al. 2014, 2015).

### 4.3 Seeds birth environments

In the top panel of Fig. 5, we show the distribution of formation redshifts of light, medium-weight, and heavy BH seeds for model R300. The bottom panel will be discussed in Section 4.5. The light-coloured histograms represent the averaged values found in 10 independent simulations and in each panel we also report the corresponding total number of BH seeds formed. The histograms in heavier colours illustrate the subsample of each family of seeds that are the progenitors of the final SMBH at  $z = 6.4$  (those systems that directly contribute to its mass assembly<sup>8</sup>). The errors associated to the number of BH seeds (and BH seeds progenitors) correspond to the difference with the maximum and minimum values found in the 10 simulations.

<sup>8</sup>As explained in Section 2.4, the progenitors of the final SMBH are seed BHs that – while growing – remain in the nuclei of their galaxies and never become wandering BHs as a consequence of minor mergers experienced by their host halo.

We find that the epoch of formation of BH seeds starts at  $z \sim 24$ , when  $\text{H}_2$  cooling in the first mini-haloes becomes efficient enough to trigger star formation.<sup>9</sup> As expected, light BH seeds form first and largely outnumber medium-weight and heavy BH seeds. On average, we find  $\sim 1831$  light BH seeds forming at  $z \geq 20$ , while  $\sim 467$  medium-weight and  $\sim 11$  heavy BH seeds form at  $16 \leq z \leq 23.5$ , when atomic-cooling haloes start to assemble. Termination of light BH seed formation is set by radiative feedback, as at  $z \leq 20$  metal-poor or pristine star-forming regions are illuminated by a supercritical LW flux (see Fig. 3) and meet the condition to form medium-weight and heavy BH seeds. We note that medium-weight seeds start to form before their heavy counterparts. Indeed, while the latter preferentially form in pristine haloes, the former can seed haloes that have already experienced previous episodes of star formation but whose  $Z$  and  $\mathcal{D}$  still meet the conditions required to form medium-weight seeds.

The above results can be compared to Valiante et al. (2016b, see in particular their fig. 4). While the results of the above study are qualitatively similar, our inhomogeneous treatment of chemical and radiative feedback leads to an increase in the absolute number of light seeds ( $\sim 830$  light and  $\sim 10$  heavy BH seeds were predicted to form, on average, in Valiante et al. 2016b) and to a more uniform distribution in the formation epoch of heavy BH seeds (the majority of which were expected to form at  $z \sim 16$  in Valiante et al. 2016b) because of the higher number of pristine regions and to the fluctuations in the LW flux.

The comparison between the lighter and darker histograms in each panel shows that the formation redshift distributions of BH seeds progenitors follow the same trend of their parent populations but with smaller numbers: on average, only  $\sim 12$ – $13$  per cent of medium-weight and light and  $\sim 27$  per cent of heavy BH seeds are progenitors of the final SMBH.

As a final remark, we stress that these absolute numbers quantify the seeds populations within a comoving volume of  $50 \text{ Mpc}^3$  selected to host a  $10^{13} M_{\odot}$  DM halo at  $z = 6.4$ . Hence, it is not straightforward to interpret these numbers as representative of an average cosmic region of the Universe. Rather, they should be considered as the expected BH population along the formation route of each  $z > 6$  SMBH.

### 4.4 Nuclear BH mass evolution

In the left-hand panel of Fig. 6, we show the resulting evolution of the nuclear BH mass as a function of redshift for model R300. This is obtained by summing over all BH seed progenitors masses<sup>10</sup> present at each redshift in the nuclei of the simulated galaxies, starting from the multiplicity of small systems hosted in minihaloes at  $z = 24$ , down to the single  $10^{13} M_{\odot}$  halo at  $z = 6.4$ . The figure shows the average evolution found among 10 different simulations considering accretion (the black line) and illustrates the separate contributions to the total mass growth of light (the blue line), medium-weight (the yellow line), and heavy (the red line) BH seed progenitors, without

<sup>9</sup>According to Valiante et al. (2016b), the fraction of metal-free gas that is able to cool in one dynamical time,  $f_{\text{cool}}$  (see equation 1), rapidly drops to zero when  $T_{\text{vir}} < 2000 \text{ K}$  at  $z \geq 25$ , even when  $J_{\text{LW}} = 0$  (see the top left-hand panel in fig. A1 of Valiante et al. 2016b). This limit corresponds to a minimum halo mass that can host star formation of  $\sim 10^6 M_{\odot}$  at  $z \sim 24$ , consistent with our resolution mass in the merger tree simulations.

<sup>10</sup>It is important to stress that we restrict the analysis to real SMBH progenitors, meaning that we reconstruct the mass and redshift distributions of all the nuclear BHs that contribute to the final SMBH mass.

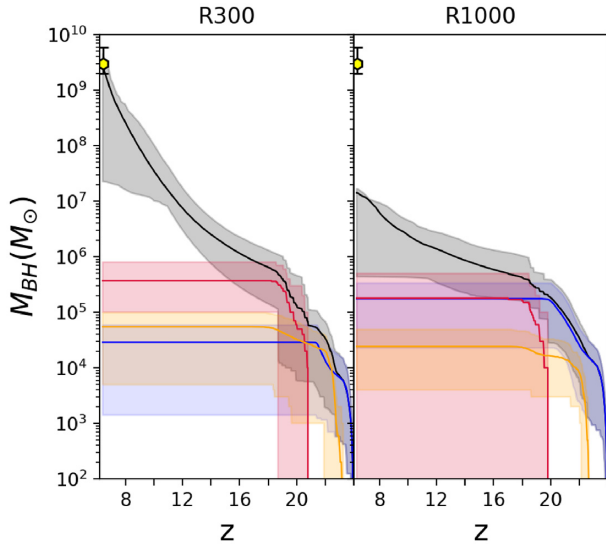


**Figure 6.** Evolution of the total mass of nuclear black holes as a function of redshift (the black line) with the separate contributions of light (the blue line), medium-weight (the yellow line), and heavy BH seed (the red line) progenitors. Each line represents the average value among 10 simulations, with the shaded region ranging between the minimum and maximum value found at each redshift. We compare the results for the same reference set of parameters but assuming  $J_{\text{cr}} = 300$  (model R300, left-hand panel) and  $J_{\text{cr}} = 1000$  (model R1000, right-hand panel). The data point at  $z = 6.4$  represents the estimated SMBH mass of the QSO J1148 that we have assumed as a prototypical system and against which we have calibrated the model free parameters.

taking into account their subsequent growth by gas accretion. For each of these lines, the shaded area with the same colour ranges between the minimum and maximum values found at each redshift.

As expected from Fig. 5, the sequence of coloured lines reflects the formation redshifts of the three BH seeds populations. Despite their smallest number, the greatest contribution to the mass growth is provided by heavy seeds, (with a cumulative BH mass of  $\sim 3 \times 10^5 M_{\odot}$ ), which is much larger than those of light ( $\sim 3 \times 10^4 M_{\odot}$ ) and medium-weight seeds ( $\sim 5 \times 10^4 M_{\odot}$ ). At  $z < 16$ , BH seeds no longer form and the growth of nuclear BHs is entirely driven by gas accretion, which provides the dominant contribution to the final SMBH mass of  $\sim 3 \times 10^9 M_{\odot}$ .

The above findings appear to be in very good qualitative agreement with the results obtained by Valiante et al. (2016b, see in particular their fig. 3), where they also find that the Eddington-limited growth of  $z \sim 6$  SMBHs relies on the formation of a small number of heavy seeds (with a total BH mass of  $\sim 10^6 M_{\odot}$ ) at early times and is dominated by gas accretion at late times. While this study confirms this qualitative picture, it also shows that medium-weight BH seeds appear to be more frequent than heavy seeds among the ancestors of  $z \sim 6$  SMBHs but – due to their smaller BH masses – their contribution to the total mass growth is largely subdominant.

#### 4.5 Dependence on the critical LW flux

The results presented above have been obtained selecting the environmental conditions to plant the three families of BH seeds according to a set of parameters that characterizes the reference model (see Table 2). Here, we wish to explore the sensitivity of our results to the adopted critical value of  $J_{\text{cr}}$ . Indeed, the critical value of the LW flux for heavy (and medium weight) BH seed formation is admittedly

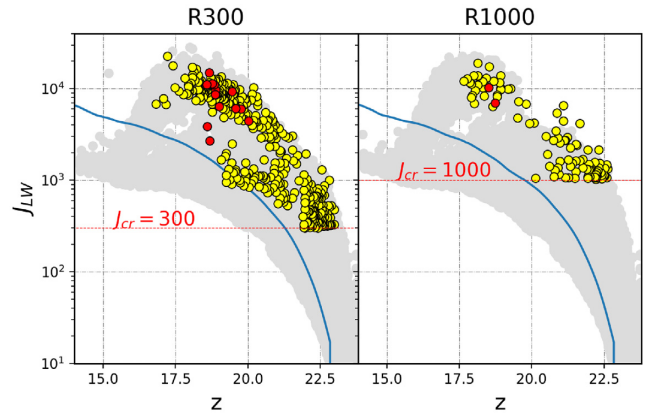


**Figure 7.** Same as Fig. 3 but for a single simulation and comparing the results of the reference model with  $J_{\text{cr}} = 300$  (model R300, left-hand panel, i.e. run 1 of Fig. 3) and  $J_{\text{cr}} = 1000$  (model R1000, right-hand panel).

very uncertain. The recent review by Inayoshi et al. (2019) provides a thorough discussion of the various results that have been found by different groups using one-zone models or full 3D simulations. In general, the value of  $J_{\text{cr}}$  depends on the details of the calculation of the optically thick  $\text{H}_2$  photodissociation rate, which is challenging even in one-zone models. Using emissivity properties that are realistic for low-metallicity galaxies, Sugimura et al. (2014) have provided the most complete calculations, finding  $J_{\text{cr}}$  to vary in the range  $\sim 1000$ – $1400$ , with the lower end that is generally favoured when self-shielding and non-LTE effects are considered (Wolcott-Green et al. 2017, 2020). Full 3D simulations, that account for dynamical effects but generally implement simplified treatments of the shielding factor, tend to find values of  $J_{\text{cr}}$  that are a factor of few higher than in one-zone models (see Inayoshi et al. 2019 and references therein).

To explore the impact of this parameter on our results, we have run a set of new simulations of the reference model adopting the increased value of  $J_{\text{cr}} = 1000$  (model R1000), as suggested by Sugimura et al. (2014). A comparison between model R1000 and the reference simulation (model R300) is provided in Figs 5, 6, and 7.

A major difference between the two models is the decrease in the number of medium-weight and heavy BH seeds in model R1000 (by a factor of  $\sim 3.3$ – $5.5$ ), partly compensated by a comparable increase of light BH seeds (see Fig. 5). Indeed, a larger  $J_{\text{cr}}$  implies a less effective radiative feedback and that star formation in metal-free or metal-poor systems, that rely on  $\text{H}_2$  cooling, is no longer suppressed (i.e. all systems exposed to  $300 < J_{\text{LW}} < 1000$  can form stars in R1000). Yet, due to the fluctuations of the LW radiation, haloes that host the formation of a medium-weight or heavy BH seeds can be illuminated by a LW flux that largely exceeds  $J_{\text{cr}}$ . This is clearly shown in Fig. 7, which is the analogous of Fig. 3, but comparing the results of a single simulation in models R300 (left-hand panel) and R1000 (right-hand panel). In model R300, a large fraction of medium-weight seeds and all heavy BH seeds is predicted to form in systems illuminated by a LW intensity  $> 2000$ . Hence, their formation should only be mildly affected by an increase in  $J_{\text{cr}}$  from 300 to 1000. However, the strong interplay between radiative and chemical feedback at these redshifts is such that the less effective radiative feedback leads to an increase in the (Pop III) SFR and to a more efficient metal and dust enrichment at these epochs. Due to star formation in their progenitors, most of the haloes that host the formation of a medium-weight or heavy BH seed in model R300 are already too enriched in model R1000 and no longer meet the conditions to form a BH seed.

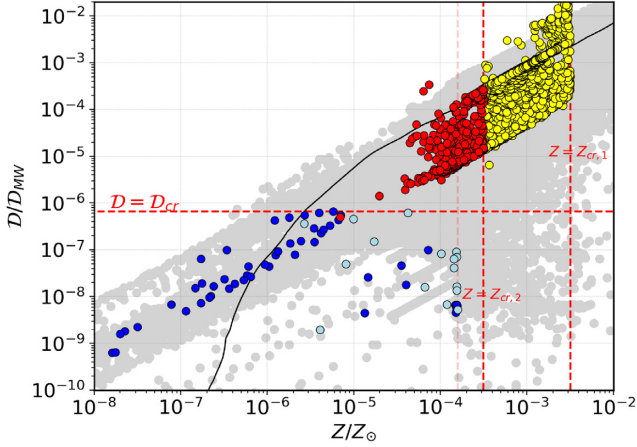


**Figure 8.** Same as Fig. 4 but for the set of parameters characterizing the SCA model and assuming  $J_{\text{cr}} = 300$  (model SCA300). The red-dashed lines are the critical dust-to-gas ratio and metallicity thresholds adopted in the SCA model (see Table 2). The thin vertical line shows the metallicity threshold adopted in the reference model (see Fig. 4 and Table 2).

Similar considerations apply if we restrict the analysis to the population of BH seed progenitors, represented by the darker coloured histograms in the bottom panels of Fig. 5. The increased value of  $J_{\text{cr}}$  in model R1000 leads to an increase by a factor  $\sim 5$  in the number of light BH seed progenitors and to a factor  $\sim 2.2$ – $3$  reduction in the number of medium-weight and heavy BH seed progenitors with respect to model R300. As a result, Fig. 6 shows that the Eddington-limited growth of the BH seed progenitors formed in model R1000 leads to the formation of a  $z \sim 6$  SMBH with an average mass of only  $\sim 2 \times 10^7 M_{\odot}$ , although with a large scatter between different simulations. In addition, the relative contributions of the three families of BH seed progenitors change and the total mass contributed by light BH progenitors is larger than that provided by medium-weight progenitors and comparable to that provided by heavy seeds.

#### 4.6 Effects of supercompetitive accretion

As anticipated in Section 3.2, we have also investigated the effects of the recently proposed SCA model (Chon & Omukai 2020). In this model, SMSs leading to medium-weight and heavy BH seeds may continue to form at higher metallicities than assumed in our reference model. In particular, we have run two additional sets of simulations, models SCA300 and SCA1000, where we have adopted the initial conditions of the SCA model summarized in Table 2 and two different values for  $J_{\text{cr}}$  (300 and 1000, respectively). The results of these two additional models are illustrated in Figs 8, 9, 10, and 11.

We first compare the results of model SCA300 with the corresponding reference run, R300. Note that, in order to ensure that the model reproduces the observed properties of our target quasar J1148 at  $z = 6.4$ , we reduced the BH accretion efficiency,  $\alpha_{\text{BH}}$ , from 150 (in the reference models) to 80 (in SCA models), as reported in Table 1.

Fig. 8 shows non-pristine formation sites of the different seed populations in one single simulation of the SCA300 model, to be compared with the R300 results in Fig. 4. The vertical and horizontal lines indicate the critical metallicity and dust-to-gas ratio thresholds adopted in the SCA model. As a consequence of the different conditions for their formation, both medium-weight and heavy seeds can form in a larger number of haloes. Since in the SCA

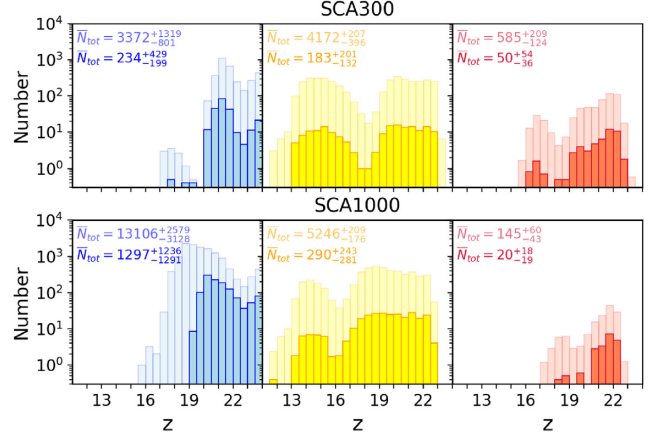


**Figure 9.** Same as Fig. 5 but for the set of parameters characterizing the SCA model and assuming  $J_{\text{cr}} = 300$  (model SCA300, top panels) and  $J_{\text{cr}} = 1000$  (model SCA1000, bottom panels).

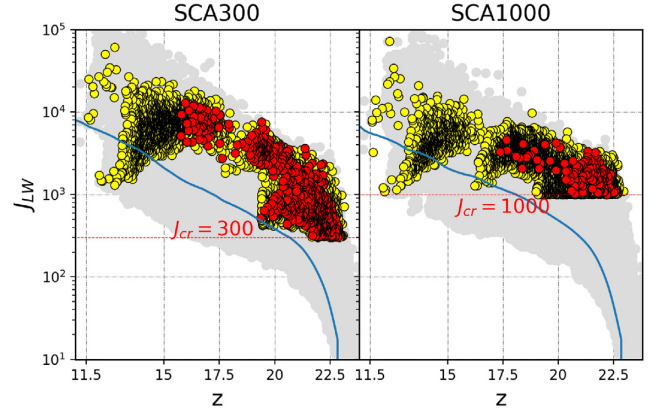


**Figure 10.** Same as Fig. 7 but for the set of parameters characterizing the SCA model and assuming  $J_{\text{cr}} = 300$  (model SCA300, left-hand panel) and  $J_{\text{cr}} = 1000$  (model SCA1000, right-hand panel).

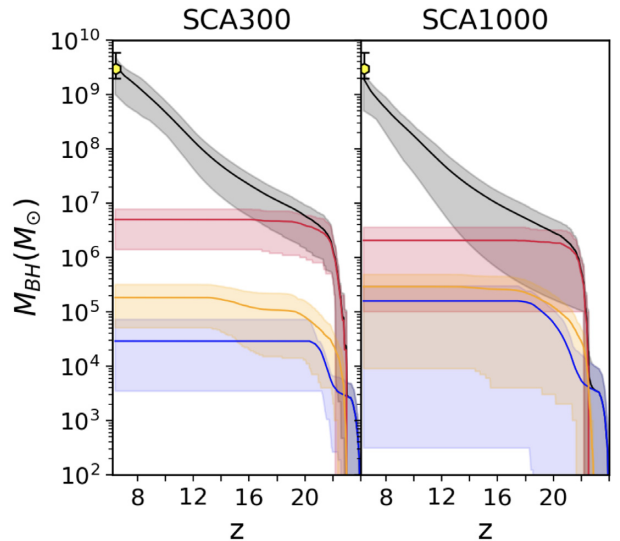


**Figure 11.** Same as Fig. 6 but for the set of parameters characterizing the SCA model and assuming  $J_{\text{cr}} = 300$  (model SCA300, left-hand panel) and  $J_{\text{cr}} = 1000$  (model SCA1000, right-hand panel).

model dust-driven fragmentation does not prevent the formation of heavy seeds, some of the sites that were originally hosting middle-weight seeds in R300 can now lead to the formation of heavy seeds. This, however, does not reduce the number of medium-weight seeds as their formation can now occur in more metal-enriched haloes compared to the reference model.

Fig. 9 shows how the looser constraints on metallicity and dust-to-gas ratio in their birth clouds lead to a significant increase in the number of medium-weight and heavy BH seeds, compared to the reference model (by a factor of  $\sim 9$  and 53, respectively). This increase is particularly dramatic for medium-weight BH seeds that become more numerous than light BH seeds in this model. The number of light BH seeds also increases (by a factor of  $\sim 1.8$ ), but this is an indirect effect of a decrease in the LW background intensity (compare the left-hand panels of Figs 7 and 10). Indeed, a large fraction of haloes that were assumed to form Pop II stars in model R300 host the formation of medium-weight BH seeds in model SCA300, leading to a decrease of the emitted LW radiation and hence of the global radiative feedback. This decrease favours the formation of Pop III stars and light BH seeds compared to model R300. At the same time, the decrease in  $J_{LW}$  (and its fluctuations) does not compromise the formation of medium-weight and heavy BH seeds that can occur in gas with higher metallicity in the SCA model. Figs 9 and 10 show that in model SCA300 the formation of medium-weight and heavy seeds extends to lower redshift and is hosted in haloes illuminated by lower  $J_{LW}$  compared to model R300.

Similar considerations apply if we restrict the analysis to BH seed progenitors: the darker coloured histograms in Fig. 9 show that they follow the same redshift distribution of their parent BH populations. Compared to model R300, the number of medium-weight and heavy BH seed progenitors formed in model SCA300 increases by a factor  $\sim 3.3$  and 16.6, respectively.

The results change when the value of  $J_{cr}$  is increased to 1000, as in model SCA1000: compared to model SCA300, the total number of medium-weight seeds mildly increases, heavy seeds are a factor of  $\sim 4$  less numerous, and the number of light seeds increases by a factor of  $\sim 3.8$ . Hence, in this case, the milder radiative feedback favours Pop III star formation, and the associated metal enrichment disfavours the formation of heavy BH seeds. The BH seed progenitor populations are also affected, with heavy BH seeds being a factor  $\sim 2.5$  less numerous than in model SCA300, while medium-weight and light BH seed progenitors increasing by  $\sim 1.6$  and  $\sim 5.5$ , respectively.

It is interesting to see how these differences affect the nuclear BH growth. A comparison between Figs 6 and 11 shows that the more favourable conditions to heavy and medium-weight seeds formation in SCA models lead to the successful growth of a  $\sim 10^9 M_\odot$  SMBH at  $z \sim 6$ , independently of the adopted value of  $J_{cr}$ . Despite the total BH mass contributed by medium-weight seeds is one order of magnitude higher than in the R300 and R1000 models, the results of SCA models confirm that the dominant mass contribution is provided by the less numerous but more massive heavy seeds.

#### 4.7 A composite picture: quality not quantity

The analysis presented above highlights how sensitive the genealogy of  $z \sim 6$  SMBHs is to BH seeds birth conditions. We find that the roots of the family tree are populated by light, medium-weight, and heavy BH ancestors, but their relative number and frequency is very sensitive to the combination of metallicity, dust-to-gas mass ratio, and illuminating LW flux that are assumed to provide the right conditions for their formation.

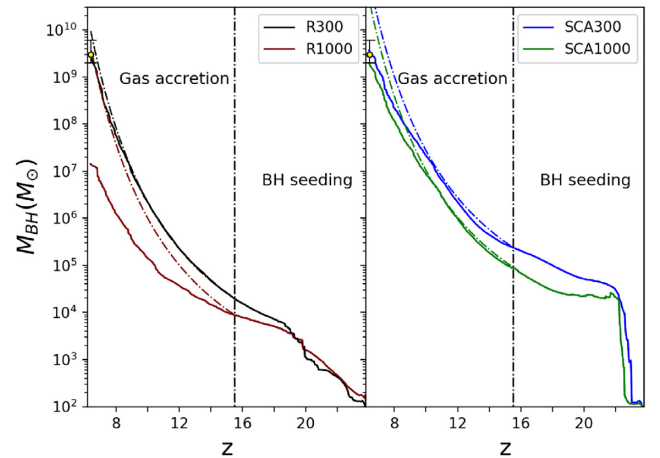


**Figure 12.** Left-hand panel: evolution of the mean BH mass as a function of redshift in models R300 (black), R1000 (red). Each line is the average value among 10 simulations. The vertical line indicates the epoch when seed formation terminates at  $z \sim 15.5$ . Below this redshift, nuclear BHs mostly grow by gas accretion. We compare the mean BH mass growth predicted by GQd models (the solid lines) with the growth histories of BHs with a mass equal to the mean nuclear BH mass at  $z \sim 15.5$  if these were assumed to grow uninterruptedly at the Eddington rate (the dashed lines). Right-hand panel: same as in the left-hand panel but for models SCA300 (blue) and SCA1000 (green).

At early times, when  $z \geq 16$ , the evolution is dominated by BH seeding and the family tree that emerges can be densely populated, with a total mass in nuclear BHs that can be larger than  $\sim 10^6 M_\odot$ . However, we also find that a successful SMBH growth history relies on the quality of its BH seeds progenitors rather than on their quantity. Indeed, more than 99 per cent of the final SMBH mass must come from gas accretion, that drives the evolution at later times, when  $z < 16$ .

In our Eddington-limited accretion scenario, BHs grow at the Bondi rate that is very sensitive to BH mass (see equation 9). Hence, for the same total mass of BH seeds formed, family trees where the BH seeds mass distribution is more top heavy and the mean BH mass is larger are better equipped to grow to a  $> 10^9 M_\odot$  SMBH.

This is illustrated in Fig. 12, where we show the evolution of the mean BH mass as a function of redshift for the reference and SCA models, adopting two different values of the critical LW flux ( $J_{cr} = 300$  and 1000).

As expected, at early times, during the BH seeding phase, the mean BH mass is strongly affected by the relative weight of different BH populations.

At the end of the BH seeding phase, the different seed BH mass distributions lead to mean BH masses that range between  $\sim 10^4 M_\odot$  for model R1000 to  $3 \times 10^5 M_\odot$  for model SCA300. During the early phase of the accretion-dominated evolution, a successful SMBH growth history requires rapid mass growth, close to the Eddington rate. To emphasize this point, for each model variant, the dashed lines show what would be the evolution if a single BH with a mass equal to the mean BH mass at  $z \sim 16$  were assumed to evolve by growing uninterruptedly at the Eddington rate. The comparison between the solid and dashed lines, for each model, shows that with exception of model R1000, the mean BH mass initially grows very close or at the Eddington rate, and becomes sub-Eddington during the late phase of the evolution, at  $z < 10$ –12.

Fig. 13 shows the mean BH accretion rate as a function of redshift for the four models. During the BH seeding epoch, at  $z \geq 15.5$ , the

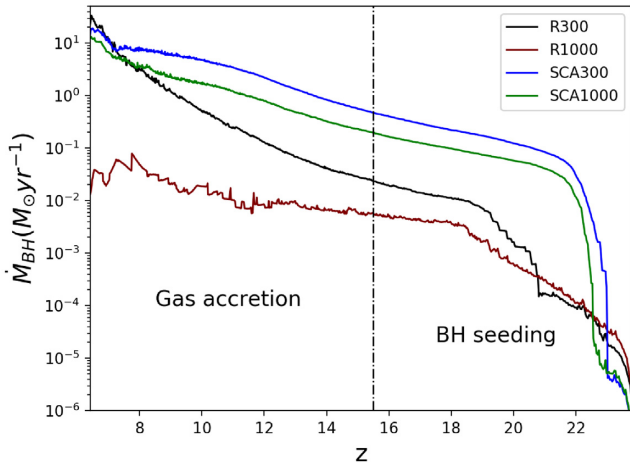


**Figure 13.** Evolution of the mean BH accretion rate as a function of redshift in models R300 (black), R1000 (red), SCA300 (blue), and SCA1000 (green). Each line is the average value among 10 simulations. The vertical line indicates the epoch when seed formation terminates, at  $z \sim 15.5$ .

accretion rates are affected by the evolving mass distribution of BH seeds progenitors. At all but the lowest redshifts, SCA models are characterized by the largest mean BH accretion rates, reflecting their larger mean BH mass. In model R300, the accretion rate increases more steeply than in SCA models, as a result of the larger gas mass in progenitor haloes, that are less affected by AGN feedback. Finally, in model R1000 the mean accretion rate never exceeds  $0.1 M_{\odot}/\text{yr}$  and shows a larger stochasticity, reflecting the smaller mean BH masses and the lower number of BH seeds in this model.

This result can be understood by looking at the mass distributions of BH seed progenitors that characterize the four models at the end of the BH seeding epoch. Fig. 14 shows the average distribution over 10 simulations at  $z = 15.5$ . At the end of the BH seeding epoch, some BH progenitors have merged to form higher mass systems (i.e. the BHs in range  $10^4 < M_{\text{BH}}/M_{\odot} < 10^5$  or with  $M_{\text{BH}} \geq 10^5 M_{\odot}$ ). The vertical lines in each panel indicate the mean BH mass, whereas the numbers refer to the total mass and number of BHs with  $M_{\text{BH}} \geq 10^5 M_{\odot}$ . These are the systems that drive the mass growth in the accretion-dominated phase at  $z < 15.5$ . In models R300 and R1000, the number and total mass of BHs in this mass range is a factor of  $\sim 10$  smaller than in models SCA300 and SCA1000, reflecting the difference in heavy BH seeds birth rate among these models. While in model R300 the enhanced accretion efficiency can counterbalance this large discrepancy, in R1000 the subsequent growth rate is too slow and leads to a final nuclear BH mass  $\sim 2 \times 10^7 M_{\odot}$  at  $z = 6.4$ , as shown by right-hand panels of Figs 6. To appreciate the large variety of possible growth histories among the different simulations, for each of the four models we report in the Appendix the BH mass evolution in each of the 10 runs, highlighting the contribution of light, medium-weight, and heavy BH seed progenitors.

## 5 DISCUSSION

Investigating the origin and growth history of  $z \geq 6$  SMBHs is very challenging. While a number of studies have been devoted to explore BH seed formation (Valiante et al. 2017) and their subsequent evolution through mergers and gas accretion (Inayoshi et al. 2019), an ab initio, self-consistent theory is still lacking.

Large-scale cosmological simulations such as MassiveBlack (Di Matteo et al. 2012), Illustris (Vogelsberger et al. 2014), EAGLE

(Schaye et al. 2015), MassiveBlack-II (Khandai et al. 2015), and BlueTides (Feng et al. 2016) have been able to achieve good agreement with observations by implementing subgrid prescriptions for BH seed formation, which generally adopt a fixed BH seed mass that is planted in haloes above a given mass threshold. In these approaches, both the BH seed mass and the minimum halo mass are free parameters of the simulation. More recently, attempts have been made to include in smaller scale cosmological simulations or in zoom-in/constrained simulations more physically motivated prescriptions for BH seeding (Bellovary et al. 2011; Habouzit, Volonteri & Dubois 2017; Tremmel et al. 2017; Huang et al. 2020). Yet, the exploration of different seed physical parameters or their growth history is still too computationally expensive, despite attempts being made to avoid this limitation through post-processing methods (DeGraf & Sijacki 2020).

Here, we have followed a complementary approach and have used semi-analytical models to run independent evolutionary histories of a  $10^{13} M_{\odot}$  DM halo at  $z = 6.4$ , following the evolution of its baryonic content since the onset of star and black hole formation at  $z = 30$ . Building on a number of previous studies (Valiante et al. 2011, 2014, 2016b; Pezzulli et al. 2016; Pezzulli et al. 2017; Valiante et al. 2018a), here we have explored, for the first time, the incidence and relevance of three different BH seed populations for the early formation of SMBH. One important aspect of our investigation is that we do not restrict the analysis to a single BH seed population. Rather, we populate the roots of SMBHs family trees with light, medium-weight, and heavy BH seeds depending on their specific birth conditions. In particular, here we have improved our previous model (Valiante et al. 2016b) by (i) introducing the possibility to form medium-weight BH seeds and by (ii) implementing a new treatment of radiative, and chemical feedback that accounts for spatial fluctuations in the metal (dust) distribution and in the LW radiation field.

Despite these new features, our main conclusions agree with previous findings, demonstrating, for the first time, that the formation of medium-weight BH seeds does not qualitatively change the growth history of the first SMBHs. Indeed, similar to Valiante et al. (2016b, 2018a), we find that, if BHs are allowed to grow without exceeding their Eddington rate, the formation of the first SMBHs at  $z > 6$  relies on a small number of heavy BH seed progenitors. At the same time, we also find that medium-weight BHs are very common among the ancestors of  $z = 6.4$  SMBHs, particularly in the SCA scenario proposed by Chon & Omukai (2020). This is in broad agreement with the pioneering work of Devecchi & Volonteri (2009) and Devecchi et al. (2012), who also investigated when and where BHs could form as a result of runaway collisions of massive stars in dense nuclear star clusters. Here, we have targeted our study to investigate the formation history of a prototypical quasar at  $z = 6.4$  instead of sampling a more representative cosmological volume. As a result, we find that despite medium-weight BHs always outnumber heavy BH seeds, their contribution to SMBH growth at  $z > 6.4$  is always subdominant with respect to that of heavy BH seeds.

One important caveat of our analysis concerns the assumed BH seed masses. While light BH seed masses are randomly sampled from an underlying Pop III stellar mass function and are therefore characterized by a mass distribution extending from a few tens to maximum  $300 M_{\odot}$ , we have adopted a constant mass of  $10^3$  and  $10^5 M_{\odot}$  for medium-weight and heavy BH seeds, respectively. This is clearly an oversimplification, as it is expected that, depending on the physical conditions at place, medium-weight seeds may form with a range of masses extending from  $\sim 300$  to  $\sim 3000 M_{\odot}$  (Devecchi et al. 2012) or  $\sim 400$  to  $\sim 1900 M_{\odot}$  (Sakurai et al. 2017), or  $\sim 100$

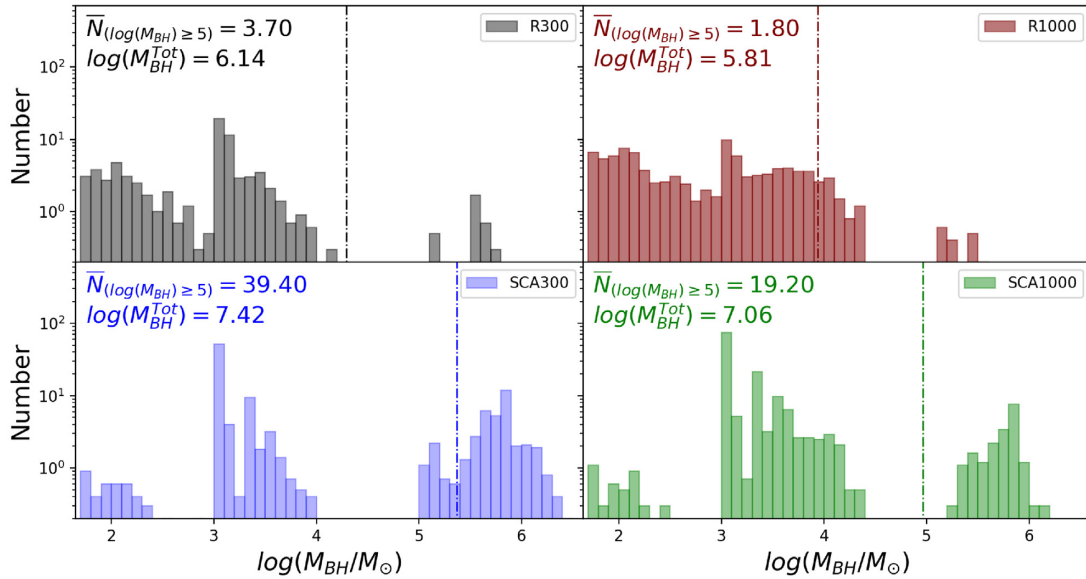


**Figure 14.** The mean BH mass function at  $z = 15.5$  averaged over 10 simulations of models R300 (top-left), R1000 (top right), SCA300 (bottom-left), and SCA1000 (bottom right). In each panel, the vertical line indicates the mean BH mass, whereas the numbers refer to the total mass and number of BHs with  $M_{BH} \geq 10^5 M_{\odot}$ .

to  $\sim 5000 M_{\odot}$  (Reinoso et al. 2020). Similarly, heavy BH seeds are also expected to span a mass range that varies between  $\sim 10^3$  to  $[3-5] 10^5 M_{\odot}$  (Lodato & Natarajan 2007), or  $\sim 5 \times 10^5$  and  $\sim 2 \times 10^6 M_{\odot}$  (Ferrara et al. 2014), or even to form in binary systems with masses of  $10^3-10^5 M_{\odot}$  (Chon et al. 2018). In addition, these figures may be significantly altered in the SCA scenario (Chon & Omukai 2020). Hence, the mass ranges of the three BH seed populations are not yet firmly assessed and may partly overlap, forming a continuum distribution from few tens to few  $10^5 M_{\odot}$ .

Finally, it is worth mentioning that the formation of direct collapse BHs may be driven/triggered also by the combined effect of subcritical LW radiation and dynamical heating, both contributing in suppressing fragmentation/star formation in rapidly growing pregalactic haloes, so that, in overdense regions, heavy seeds could be more common (larger number density) than previously expected (e.g. Wise et al. 2019b).

While a more refined description of the seed mass and its dependence on the birth conditions is deferred to a future study, here we anticipate that this may impact our results by changing the relative contribution of the three BH seeds populations to the mass growth of the final SMBH. More indirectly, it may also modify the baryonic evolution of their host galaxies and hence the relative frequency of medium-weight and heavy BH seeds that form at later times. Yet, our results suggest that, for each SMBH in place at  $z = 6.4$ , a large number of BH seeds form at  $z > 15-16$  (see Figs 5 and 9), only a small fraction of which are the progenitors of the final SMBH. Another caveat of our model is that we do not consider baryonic streaming motion (BSM) that may suppress star formation in less massive haloes (typically  $T_{vir} < 10^4 K$ ), preventing gas collapse (Schauer et al. 2017; Hirano et al. 2018; Inayoshi, Li & Haiman 2018). This limitation does not have a direct impact on the formation of heavy and medium-weight BH seeds, which form in larger, atomic cooling haloes. However, the lack of star formation in mini-haloes may have an indirect effect because (i) the gas will remain chemically pristine until atomic-cooling haloes form and (ii) the suppression of  $H_2$  cooling will be possible only by nearby star-forming atomic-cooling haloes, in the so-called ‘synchronized-halo’

model (Visbal et al. 2014). While it is not straightforward to assess the net effect of these two processes in our model, Schauer et al. (2017) argue that BSM may provide favourable conditions for the formation of heavy BH seeds. The minimum DM halo mass where gas cooling is suppressed by BSM increases ( $T_{vir} \sim 1-2 \times 10^4 K$ ) if the halo experiences a violent merger episode (Inayoshi et al. 2018). However, these events are expected to be rare, affecting less than 1 per cent of the haloes (see fig. 2 in Inayoshi et al. 2018).

## 6 SUMMARY AND CONCLUSIONS

We have investigated the role of three BH seed populations in the formation history of  $z > 6$  SMBHs. Building on previous studies, we have further extended our semi-analytical data-constrained model, GQd, by including a statistical description of the spatial fluctuations in metal and dust enrichment and in the intensity of the LW radiation field. For the first time, we have investigated the birth rate of light, medium-weight, and heavy BH seeds by selecting their formation sites according to physically motivated conditions on the metal and dust content as well as on the intensity of the illuminating LW radiation field (model R300). We find that

- (i) inhomogeneous metal and dust enrichment and fluctuations in the LW radiation favour the formation of seeds and extends their birth epoch down to  $z \sim 16$ , when the filling factor of enriched regions becomes  $Q \sim 1$ ;
- (ii) light seeds are the first to form in pristine star-forming regions, and their formation is suppressed at  $z \sim 20$  by radiative feedback that illuminates the metal-poor gas above the critical value, preventing  $H_2$ -cooling. On average,  $\sim 1831$  light seeds form in our reference model, but less than  $\sim 13$  per cent of these are true progenitors of the final SMBH;
- (iii) medium-weight and heavy BH seeds form at  $16 \leq z \leq 23.5$  when atomic cooling haloes start to assemble. Medium-weight seeds form in metal-poor star-forming regions illuminated by a LW radiation  $J_{cr} < J_{LW} < 100 J_{cr}$  from neighbouring systems, while

heavy seeds mostly form in pristine regions when the illuminating LW intensity reaches values  $10 J_{\text{cr}} < J_{\text{LW}} < 100 J_{\text{cr}}$ . On average,  $\sim 467$  medium-weight and  $\sim 11$  heavy seeds form in the reference model,  $\sim 12 - 27$  per cent of which are SMBH progenitors;

(iv) despite their smaller number, heavy BH seed progenitors provide the largest contribution to the SMBH mass growth, with a cumulative mass of  $\sim 3 \times 10^5 M_{\odot}$  and triggering efficient gas accretion, that drives the mass growth at  $z < 16$  and leads to the formation of a  $\sim 3 \times 10^9 M_{\odot}$  SMBH at  $z = 6.4$ . For most of the time, the average gas accretion rate is very close to Eddington.

We have explored the sensitivity of the above results to variations of the adopted critical value of the LW flux by running a set of simulations with  $J_{\text{cr}} = 1000$  (R1000). We find that

(i) a larger  $J_{\text{cr}}$  has the effect of reducing the strength of radiative feedback, favouring Pop III star formation and increasing the number of light seeds (by a factor  $\sim 5$ ). However, this also causes a more efficient metal and dust enrichment, which limits the formation of medium-weight and heavy black hole seeds, decreasing their number by a factor  $\sim 3.3-5.5$ . A similar decrease (by a factor of  $\sim 2.2-3$ ) is also found in the number of medium-weight and heavy seed progenitor. This has a large impact on the formation of the SMBH, which on average reaches a mass of  $\sim 2 \times 10^7 M_{\odot}$  by  $z = 6.4$ , with a large dispersion of values among different evolutionary histories.

Finally, we have explored the possibility to form SMSs – leading to medium-weight and heavy BH seeds - at higher metallicity than assumed in our reference model because of SCA (Chon & Omukai 2020). We find that

(i) the looser constraints on metallicity and dust-to-gas ratio in the birth clouds predicted by this model (SCA300) lead to a significant increase in the total number of medium-weight (by a factor  $\sim 9$ ) and heavy (by a factor  $\sim 50$ ) BH seeds; the number of light seeds also increases (by a factor  $\sim 2$ ) due to the lower intensity of the LW background and the milder radiative feedback induced by a more significant contribution to the LW emissivity by accreting BHs, which are less efficient sources compared to Pop II stars. Heavy seeds dominate the mass growth, leading to the formation of a  $\sim 3 \times 10^9 M_{\odot}$  SMBH at  $z = 6.4$ , even when the critical intensity of the LW background is increased to  $J_{\text{cr}} = 1000$  (SCA1000).

In the Eddington-limited accretion scenario that we have explored, we find that a successful SMBH growth history relies on the quality of its BH progenitors, rather than on their quantity: family trees whose roots are seeded by a sufficient number of heavy BH progenitors are better suited to grow  $> 10^9 M_{\odot}$  SMBHs by  $z = 6.4$ .

Our study suggests that the genealogy of  $z \sim 6$  SMBHs is characterized by a rich variety of BH progenitors, which represent only a small fraction ( $< 10-20$  per cent) of all the BHs that seed galaxies at  $z > 15.5$ . While their mass distribution depends on the physical conditions (metallicity, dust-to-gas ratio, illuminating LW radiation) at their birth, these properties need to be explored in the attempt of making a census of the BH population at high- $z$ . This study is a first attempt to describe the richness of the BH landscape at cosmic dawn that may be explored by future electromagnetic and gravitational wave facilities.

## ACKNOWLEDGEMENTS

We thank the Referee for her/his careful reading of the manuscript and insightful comments.

We acknowledge support from the Amaldi Research Center funded by the MIUR program ‘Dipartimento di Eccellenza’ (CUP:B8I118001170001), from the INFN TEONGRAV specific initiative, and the networking support by the COST Action CA16104.

This work is partially supported by the National Science Foundation of China (11721303, 11991052, 11950410493), the National Key Research and Development Program of China (2016YFA0400702).

KO and SC acknowledge financial support by the Grants-in-Aid for Basic Research by the Ministry of Education, Culture, Sports, Science and Technology of Japan (SC:19J00324, KO:25287040, 17H01102, 17H02869).

FS thanks the University of Zürich for the kind support and hospitality and acknowledges the precious exchange of opinions and helpful advice of participants to the São Paulo School of advanced science on FIRST LIGHT and XXXI Canary Islands Winter School of Astrophysics.

## DATA AVAILABILITY

The simulated data underlying this article will be shared on reasonable request to the corresponding author. The code GQD is not publicly available. The adopted approach and further possible improvements can be discussed with the corresponding author and the other code developers/users within the working group.

## REFERENCES

- Ade P. A. et al., 2014, *A&A*, 571, A16  
 Agarwal B., Khochfar S., Johnson J. L., Neistein E., Dalla Vecchia C., Livio M., 2012, *MNRAS*, 425, 2854  
 Agarwal B., Regan J., Klessen R. S., Downes T. P., Zackrisson E., 2017, *MNRAS*, 470, 4034  
 Ahn K., Shapiro P. R., Iliev I. T., Mellema G., Pen U.-L., 2009, *ApJ*, 695, 1430  
 Amaro-Seoane P., Santamaria L., 2010, *ApJ*, 722, 1197  
 Baldassare V. F., Dickey C., Geha M., Reines A. E., 2020, *ApJ*, 898, L3  
 Ballone A., Mapelli M., Pasquato M., 2018, *MNRAS*, 480, 4684  
 Bañados E. et al., 2016, *ApJS*, 227, 11  
 Bañados E. et al., 2018, *Nature*, 553, 473  
 Barack L. et al., 2019, *Class. Quantum Gravity*, 36, 143001  
 Barrows R. S., Mezcua M., Comerford J. M., 2019, *ApJ*, 882, 181  
 Becerra F., Greif T. H., Springel V., Hernquist L. E., 2015, *MNRAS*, 446, 2380  
 Becerra F., Marinacci F., Bromm V., Hernquist L. E., 2018, *MNRAS*, 480, 5029  
 Bellovary J., Volonteri M., Governato F., Shen S., Quinn T., Wadsley J., 2011, *ApJ*, 742, 13  
 Bianchi S., Schneider R., Valiante R., 2009, in Henning T., Grün E., Steinacker J., eds, ASP Conf. Ser. Vol. 414, Cosmic Dust - Near and Far. Astron. Soc. Pac., San Francisco, p.65  
 Bondi H., 1952, *MNRAS*, 112, 195  
 Bondi H., Hoyle F., 1944, *MNRAS*, 104, 273  
 Bromm V., 2013, *Rep. Prog. Phys.*, 76, 112901  
 Bromm V., Loeb A., 2003, *ApJ*, 596, 34  
 Bruzual G., Charlot S., 2003, *MNRAS*, 344, 1000  
 Callegari S., Kazantzidis S., Mayer L., Colpi M., Bellovary J. M., Quinn T., Wadsley J., 2011, *ApJ*, 729, 85  
 Callegari S., Mayer L., Kazantzidis S., Colpi M., Governato F., Quinn T., Wadsley J., 2009, *ApJ*, 696, L89  
 Capelo P. R., Volonteri M., Dotti M., Bellovary J. M., Mayer L., Governato F., 2015, *MNRAS*, 447, 2123  
 Chiaki G., Marassi S., Nozawa T., Yoshida N., Schneider R., Omukai K., Limongi M., Chieffi A., 2015, *MNRAS*, 446, 2659

- Chiaki G., Schneider R., Nozawa T., Omukai K., Limongi M., Yoshida N., Chieffi A., 2014, *MNRAS*, 439, 3121
- Chon S., Hirano S., Hosokawa T., Yoshida N., 2016, *ApJ*, 832, 134
- Chon S., Hosokawa T., Yoshida N., 2018, *MNRAS*, 475, 4104
- Chon S., Omukai K., 2020, *MNRAS*, 494, 2851
- Clark P. C., Glover S. C., Klessen R. S., 2008, *ApJ*, 672, 757
- Coleman Miller M., Hamilton D. P., 2002, *MNRAS*, 330, 232
- Cubbon R. M. et al., 2007, *Eur. Heart J.*, 28, 540
- Davies M. B., Miller M. C., Bellovary J. M., 2011, *ApJ*, 740, L42
- Dayal P., Rossi E. M., Shiralilou B., Piana O., Choudhury T. R., Volonteri M., 2019, *MNRAS*, 486, 2336
- de Bressan M., Salvadori S., Schneider R., Valiante R., Omukai K., 2017, *MNRAS*, 465, 926
- de Bressan M., Schneider R., Valiante R., Salvadori S., 2014, *MNRAS*, 445, 3039
- DeGraf C., Sijacki D., 2020, *MNRAS*, 491, 4973
- Devecci B., Volonteri M., 2009, *ApJ*, 694, 302
- Devecci B., Volonteri M., Rossi E. M., Colpi M., Portegies Zwart S., 2012, *MNRAS*, 421, 1465
- Di Matteo T., Khandai N., DeGraf C., Feng Y., Croft R. A. C., Lopez J., Springel V., 2012, *ApJ*, 745, L29
- Dijkstra M., Ferrara A., Mesinger A., 2014, *MNRAS*, 442, 2036
- Dijkstra M., Haiman Z., Mesinger A., Wyithe J. S. B., 2008, *MNRAS*, 391, 1961
- Dubois Y., Volonteri M., Silk J., Devriendt J., Slyz A., Teyssier R., 2015, *MNRAS*, 452, 1502
- Fan X. et al., 2003, *AJ*, 125, 1649
- Fan X., Narayanan V. K., Strauss M. A., White R. L., Becker R. H., Pentericci L., Rix H.-W., 2002, *AJ*, 123, 1247
- Feng Y., Di-Matteo T., Croft R. A., Bird S., Battaglia N., Wilkins S., 2016, *MNRAS*, 455, 2778
- Ferrara A., Salvadori S., Yue B., Schleicher D., 2014, *MNRAS*, 443, 2410
- Frebel A., Norris J. E., 2015, *ARA&A*, 53, 631
- Graziani L., Schneider R., Ginolfi M., Hunt L. K., Maio U., Glatzle M., Ciardi B., 2020, *MNRAS*, 494, 1091
- Greene J. E. et al., 2010, *ApJ*, 721, 26
- Greif T. H., 2015, *Comput. Astrophys. Cosmol.*, 2, 3
- Gürkan M. A., Freitag M., Rasio F. A., 2004, *ApJ*, 604, 632
- Habouzit M., Volonteri M., Dubois Y., 2017, *MNRAS*, 468, 3935
- Habouzit M., Volonteri M., Latif M., Dubois Y., Peirani S., 2016a, *MNRAS*, 463, 529
- Habouzit M., Volonteri M., Latif M., Dubois Y., Peirani S., 2016b, *MNRAS*, 463, 529
- Heger A., Woosley S. E., 2002, *ApJ*, 567, 532
- Hirano S., Hosokawa T., Yoshida N., Umeda H., Omukai K., Chiaki G., Yorke H. W., 2014, *ApJ*, 781, 60
- Hirano S., Yoshida N., Sakurai Y., Fujii M. S., 2018, *ApJ*, 855, 17
- Hirano S., Zhu N., Yoshida N., Spergel D., Yorke H. W., 2015, *ApJ*, 814, 18
- Hosokawa T., Hirano S., Kuiper R., Yorke H. W., Omukai K., Yoshida N., 2016, *ApJ*, 824, 119
- Hosokawa T., Omukai K., Yorke H. W., 2012, *ApJ*, 756, 93
- Hosokawa T., Omukai K., Yoshida N., Yorke H. W., 2011, *Science*, 334, 1250
- Hoyle F., Lyttleton R. A., 1939, *Proc. Cambridge Phil. Soc.*, 35, 405
- Huang K.-W., Ni Y., Feng Y., Di Matteo T., 2020, *MNRAS*, 496, 1
- Illiev I. T., Scannapieco E., Martel H., Shapiro P. R., 2003, *MNRAS*, 341, 81
- Inayoshi K., Haiman Z., Ostriker J. P., 2016, *MNRAS*, 459, 3738
- Inayoshi K., Li M., Haiman Z., 2018, *MNRAS*, 479, 4017
- Inayoshi K., Omukai K., Tasker E., 2014, *MNRAS*, 445, L109
- Inayoshi K., Tanaka T. L., 2015, *MNRAS*, 450, 4350
- Inayoshi K., Visbal E., Haiman Z., 2020, *ARA&A*, 58, 27
- Jaacks J., Thompson R., Finkelstein S. L., Bromm V., 2018, *MNRAS*, 475, 4396
- Jiang L. et al., 2016, *ApJ*, 833, 222
- Johnson J. L., Dalla Vecchia C., Khochfar S., 2013, *MNRAS*, 428, 1857
- Katz H., Sijacki D., Haehnelt M. G., 2015, *MNRAS*, 451, 2352
- Khandai N., Di Matteo T., Croft R., Wilkins S., Feng Y., Tucker E., DeGraf C., Liu M.-S., 2015, *MNRAS*, 450, 1349
- Kim S. S., Figer D. F., Morris M., 2004, *ApJ*, 607, L123
- Kremer K. et al., 2019, *Phys. Rev. D*, 99, 063003
- Lacey C., Cole S., 1993, *MNRAS*, 262, 627
- Larson R. B., 1998, *MNRAS*, 301, 569
- Latif M. A., Schleicher D. R. G., Hartwig T., 2016, *MNRAS*, 458, 233
- Latif M. A., Schleicher D. R. G., Schmidt W., Niemeyer J. C., 2013, *MNRAS*, 436, 2989
- Lodato G., Natarajan P., 2007, *MNRAS*, 377, L64
- Lupi A., Colpi M., Devecchi B., Galanti G., Volonteri M., 2014, *MNRAS*, 3616, 1365-2966
- Lupi A., Haardt F., Dotti M., Fiacconi D., Mayer L., Madau P., 2015, *MNRAS*, 2993, 0035-8711
- Lupi A., Haiman Z., Volonteri M., 2021, *MNRAS*, 5046, 0035-8711
- Madau P., Ferrara A., Rees M. J., 2001, *ApJ*, 555, 92
- Madau P., Haardt F., Dotti M., 2014, *ApJ*, 784, L38
- Maio U., Borgani S., Ciardi B., Petkova M., 2019, *Publ. Astron. Soc. Aust.*, 36, e020
- Maio U., Khochfar S., Johnson J. L., Ciardi B., 2011, *MNRAS*, 414, 1145
- Marassi S., Chiaki G., Schneider R., Limongi M., Omukai K., Nozawa T., Chieffi A., Yoshida N., 2014, *ApJ*, 794, 100
- Matsukoba R., Takahashi S. Z., Sugimura K., Omukai K., 2019, *MNRAS*, 484, 2605
- Matsuoka Y. et al., 2019, *ApJ*, 872, L2
- Mayer L., 2017, *Nat. Astron.*, 1, 0108
- Mayer L., Bonoli S., 2019, *Rep. Prog. Phys.*, 82, 016901
- Mayer L., Fiacconi D., Bonoli S., Quinn T., Roškar R., Shen S., Wadsley J., 2015, *ApJ*, 810, 51
- Mezcua M., Civano F., Marchesi S., Suh H., Fabbiano G., Volonteri M., 2018, *MNRAS*, 478, 2576
- Miller J. M., Fabian A., Miller M., 2004, *ApJ*, 614, L117
- Muratov A. L., Gnedin O. Y., Gnedin N. Y., Zemp M., 2013, *ApJ*, 773, 19
- Nguyen D. D. et al., 2019, *ApJ*, 872, 104
- Omukai K., 2001, *ApJ*, 546, 635
- Omukai K., Hosokawa T., Yoshida N., 2010, *ApJ*, 722, 1793
- Omukai K., Nishi R., 1998, *ApJ*, 508, 141
- Omukai K., Palla F., 2003, *ApJ*, 589, 677
- Omukai K., Schneider R., Haiman Z., 2008, *ApJ*, 686, 801
- Omukai K., Tsuribe T., Schneider R., Ferrara A., 2005, *ApJ*, 626, 627
- Pallottini A. et al., 2015, *MNRAS*, 453, 2465
- Petri A., Ferrara A., Salvaterra R., 2012, *MNRAS*, 422, 1690
- Pezzulli E., Valiante R., Schneider R., 2016, *MNRAS*, 458, 3047
- Pezzulli E., Volonteri M., Schneider R., Valiante R., 2017, *MNRAS*, 471, 589
- Portegies Zwart S. F., McMillan S. L. W., 2002, *ApJ*, 576, 899
- Raiteri C. M., Villata M., Navarro J. F., 1996, *Mem. Soc. Astron. Ital.*, 67, 817
- Regan J. A., Haehnelt M. G., 2009, *MNRAS*, 396, 343
- Regan J. A., Johansson P. H., Wise J. H., 2014, *ApJ*, 795, 137
- Regan J. A., Wise J. H., O'Shea B. W., Norman M. L., 2020, *MNRAS*, 492, 3021
- Reines A. E., Volonteri M., 2015, *ApJ*, 813, 82
- Reinoso B., Schleicher D. R. G., Fellhauer M., Klessen R. S., Boekholt T. C. N., 2018, *A&A*, 614, A14
- Reinoso B., Schleicher D. R. G., Fellhauer M., Leigh N. W. C., Klessen R. S., 2020, *A&A*, 639, A92
- Reinoso B., Schleicher D., Fellhauer M., Klessen R., Boekholt T., Vergara M., Alister Seguel P., 2019, *Bol. Asoc. Argentina Astron. Plata Argentina*, 61, 154
- Robert P. F., Murphy M. T., O'Meara J. M., Crighton N. H. M., Fumagalli M., 2019, *MNRAS*, 483, 2736
- Sądowski A., R. Narayal, 2016, *MNRAS*, 456, 3929
- Sądowski A., 2009, *ApJS*, 183, 171
- Safonova M., Shastri P., 2010, *Ap&SS*, 325, 47
- Sakurai Y., Yoshida N., Fujii M. S., Hirano S., 2017, *MNRAS*, 472, 1677
- Salvadori S., Tolstoy E., Ferrara A., Zaroubi S., 2014, *MNRAS*, 437, L26
- Sarmento R., Scannapieco E., Côté B., 2019, *ApJ*, 871, 206
- Sazonov S. Y., Ostriker J. P., Sunyaev R. A., 2004, *MNRAS*, 347, 144
- Schaerer D., 2002, *A&A*, 382, 28
- Schauer A. T. P., Regan J., Glover S. C. O., Klessen R. S., 2017, *MNRAS*, 471, 4878

- Schaye J. et al., 2015, *MNRAS*, 446, 521  
 Schneider R., Omukai K., Bianchi S., Valiante R., 2012, *MNRAS*, 419, 1566  
 Sesana A., Haardt F., Madau P., Volonteri M., 2005, *ApJ*, 623, 23  
 Shakura N. I., 1973, *Sov. Astron.*, 16, 756  
 Shang C., Bryan G. L., Haiman Z., 2010, *MNRAS*, 402, 1249  
 Shen R.-F., 2019, *ApJ*, 871, L17  
 Springel V., Di Matteo T., Hernquist L., 2005, *MNRAS*, 361, 776  
 Stone N. C., Küpper A. H. W., Ostriker J. P., 2017, *MNRAS*, 467, 4180  
 Sugimura K., Matsumoto T., Hosokawa T., Hirano S., Omukai K., 2020, *ApJ*, 892, L14  
 Sugimura K., Omukai K., Inoue A. K., 2014, *MNRAS*, 445, 544  
 Tagawa H., Haiman Z., Kocsis B., 2020, *ApJ*, 892, 36  
 Takekawa S., Oka T., Iwata Y., Tsujimoto S., Nomura M., 2019, *ApJ*, 871, L1  
 Takeo E., Inayoshi K., Mineshige S., 2020, *MNRAS*, 497, 302  
 Tornatore L., Ferrara A., Schneider R., 2007, *MNRAS*, 382, 945  
 Tremmel M., Karcher M., Governato F., Volonteri M., Quinn T. R., Pontzen A., Anderson L., Bellovary J., 2017, *MNRAS*, 470, 1121  
 Valiante R. et al., 2021, *MNRAS*, 500, 4095  
 Valiante R., Agarwal B., Habouzit M., Pezzulli E., 2017, *Publ. Astron. Soc. Aust.*, 34, e031  
 Valiante R., Schneider R., Graziani L., Zappacosta L., 2018a, *MNRAS*, 474, 3825  
 Valiante R., Schneider R., Salvadori S., Bianchi S., 2011, *MNRAS*, 416, 1916  
 Valiante R., Schneider R., Salvadori S., Gallerani S., 2014, *MNRAS*, 444, 2442  
 Valiante R., Schneider R., Volonteri M., 2016a, *Publ. Astron. Soc. Aust.*, 33  
 Valiante R., Schneider R., Volonteri M., Omukai K., 2016b, *MNRAS*, 457, 3356  
 Valiante R., Schneider R., Zappacosta L., Graziani L., Pezzulli E., Volonteri M., 2018b, *MNRAS*, 476, 407  
 van den Hoek L. B., Groenewegen M. A. T., 1997, *A&AS*, 123, 305  
 Van Wassenhove S., Capelo P. R., Volonteri M., Dotti M., Bellovary J. M., Mayer L., Governato F., 2014, *MNRAS*, 439, 474  
 Vanzella E. et al., 2020, *MNRAS*, 494, L81  
 Visbal E., Haiman Z., Bryan G. L., 2014, *MNRAS*, 442, L100  
 Vogelsberger M. et al., 2014, *MNRAS*, 444, 1518  
 Volonteri M., 2010, *A&AR*, 18, 279  
 Walch S., Naab T., 2015, *MNRAS*, 451, 2757  
 Wang F. et al., 2021, *ApJ*, 907, L1  
 Willott C. J. et al., 2010, *AJ*, 139, 906  
 Willott C. J., McLure R. J., Jarvis M. J., 2003, *ApJ*, 587, L15  
 Wise J. H., Regan J. A., O’Shea B. W., Norman M. L., Downes T. P., Xu H., 2019a, *Nature*, 566, 85  
 Wise J. H., Regan J. A., O’Shea B. W., Norman M. L., Downes T. P., Xu H., 2019b, *Nature*, 566, 85  
 Wise J. H., Turk M. J., Abel T., 2008, *ApJ*, 682, 745  
 Wise J. H., Turk M. J., Norman M. L., Abel T., 2012, *ApJ*, 745, 50  
 Wolcott-Green J., Haiman Z., Bryan G. L., 2017, *MNRAS*, 469, 3329  
 Wolcott-Green J., Haiman Z., Bryan G. L., 2020, *MNRAS*, 500, 138  
 Woo J.-H., Cho H., Gallo E., Hodges-Kluck E., Le H. A. N., Shin J., Son D., Horst J. C., 2019, *Nat. Astron.*, 3, 755  
 Woosley S. E., Heger A., Weaver T. A., 2002, *Rev. Mod. Phys.*, 74, 1015  
 Woosley S. E., Weaver T. A., 1995, *ApJS*, 101, 181  
 Wu X.-B. et al., 2015, *Nature*, 518, 512  
 Xu H., Norman M. L., O’Shea B. W., Wise J. H., 2016, *ApJ*, 823, 140  
 Yang J. et al., 2020, *ApJ*, 897, L14  
 Yoshida N., Omukai K., Hernquist L., 2008, *Science*, 321, 669  
 Zhukovska S., Gail H.-P., Tieloff M., 2008, *A&A*, 479, 453

## APPENDIX A: BH MASS GROWTH

In Sections 4.4 and 4.6, we have discussed the evolution of the total mass of nuclear BHs as a function of redshift, highlighting the contribution of light, medium-weight, and heavy seeds in the R300, R1000, SCA300, and SCA1000 models. Figs 6 and 11 illustrate the trends obtained by averaging over 10 independent simulations of each model and the shaded regions represent the minimum and maximum value found at each  $z$ . The extent of these shaded regions indicates the large variety of individual evolutionary histories that we find, particularly in models R300 and R1000. In Figs A1, A2, A3, and A4, we show the results obtained in each run of R300, R1000, SCA300, and SCA1000 models.

In model R300 (Fig. A1) a similar evolution is found for the total BH mass (the black lines) among all the 10 runs, with the exception of runs (2) and (3) where the final BH mass does not exceed  $2 \times 10^8 M_{\odot}$ , as a consequence of the lower black hole accretion rate.

The relative contribution of medium-weight and light BH seed progenitors can be very different, reflecting the impact of the cosmological evolution of the host galaxies on their birth conditions. The two populations provide almost equal contributions in some simulations, e.g. (9), or largely different ones in other, such as run (7), where only a few light BH seed progenitors form.

A completely different scenario is found in model R1000, where in all the runs the final SMBH is  $< 10^8 M_{\odot}$  at  $z = 6.4$ . This is a consequence of the smaller number (or absence, such as in run 3) of heavy BH seed progenitors formed and of their lower accretion rates. Indeed, a larger  $J_{\text{cr}}$  leads to milder radiative feedback and to more efficient (Pop III) star formation, increasing the number of light BH seed progenitors and decreasing the amount of gas that feeds BH growth. In 5 of 10 simulations, the total mass contributed light BH seeds is comparable or exceeds the one provided by heavy or medium-weight progenitors.

The 10 runs of the SCA300 (Fig. A3) and SCA1000 (Fig. A4) models show similar evolutionary histories, with significantly larger numbers of medium-weight and heavy seed progenitors, with respect to R300 and R1000. This reflects the looser constraints set by SCA models on the formation of SMSs. An SMBH  $> 5 \times 10^8 M_{\odot}$  is predicted at  $z = 6.4$  in all cases and (almost) independently of the adopted  $J_{\text{cr}}$  threshold.

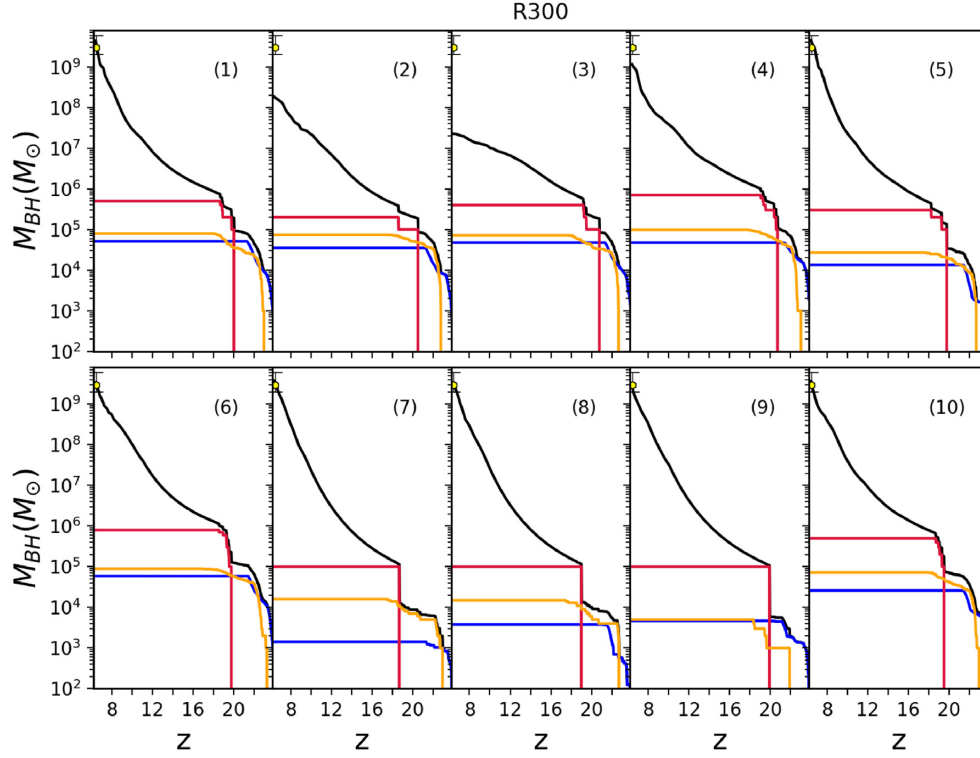


**Figure A1.** Evolution of the total mass of nuclear black holes as a function of redshift (the black line) with the separate contributions of light (the blue line), medium-weight (the yellow line), and heavy BH seed (the red line) progenitors. Each panel shows individual results over 10 simulations for R300 model.

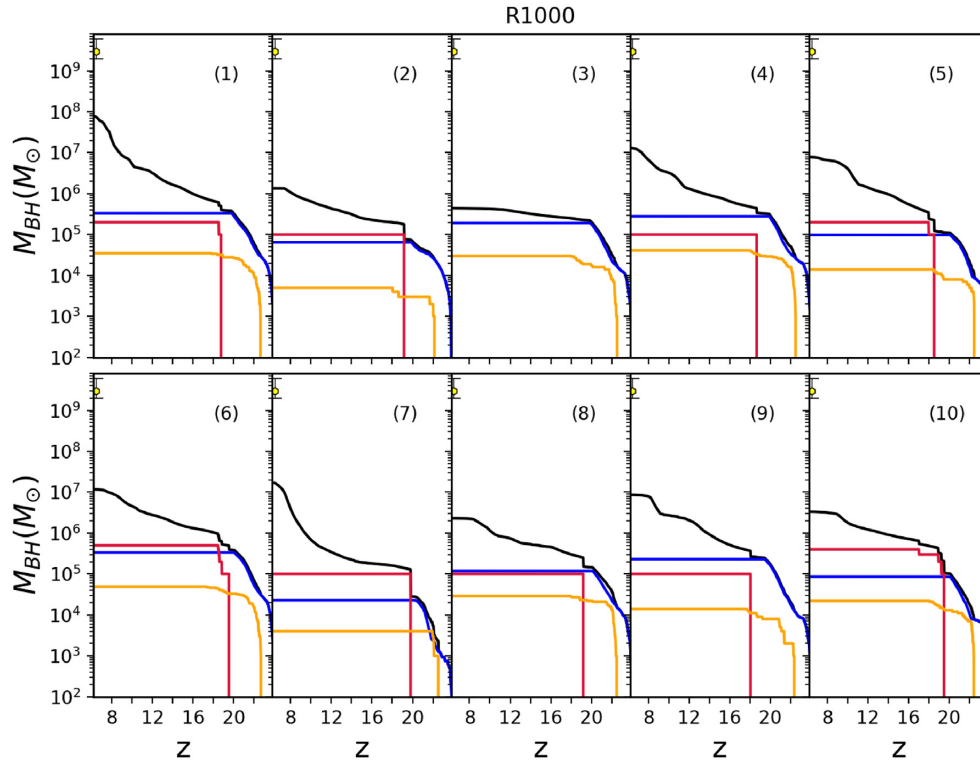


**Figure A2.** Same as Fig. A1 but for model R1000.

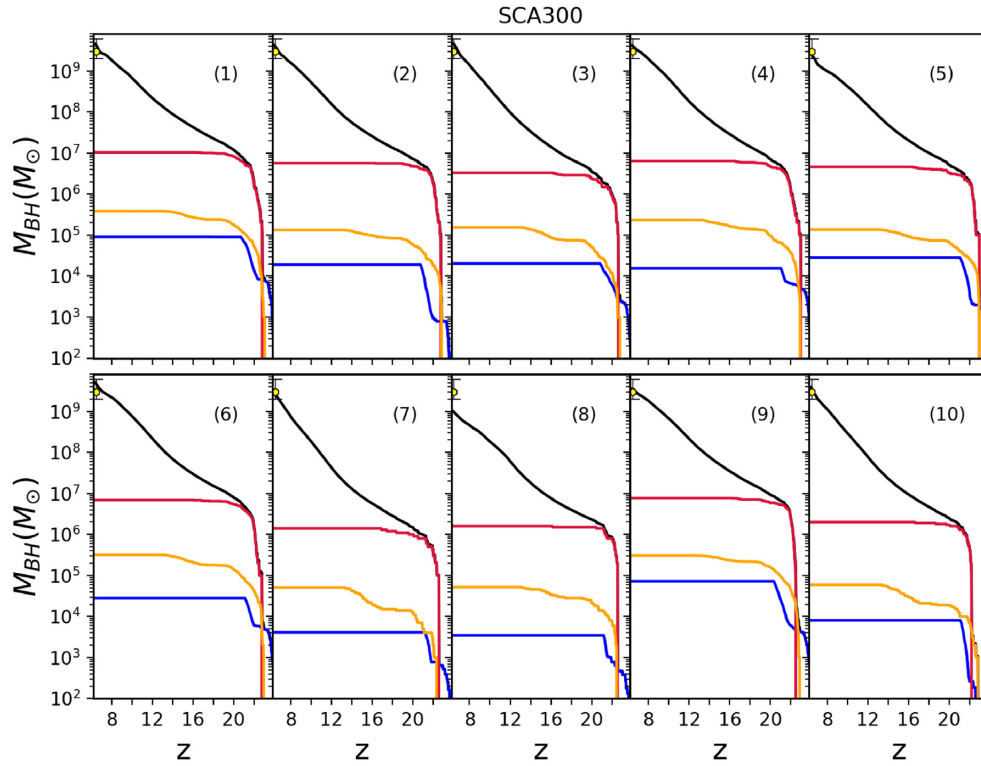


**Figure A3.** Same as Fig. A1 but for model SCA300.

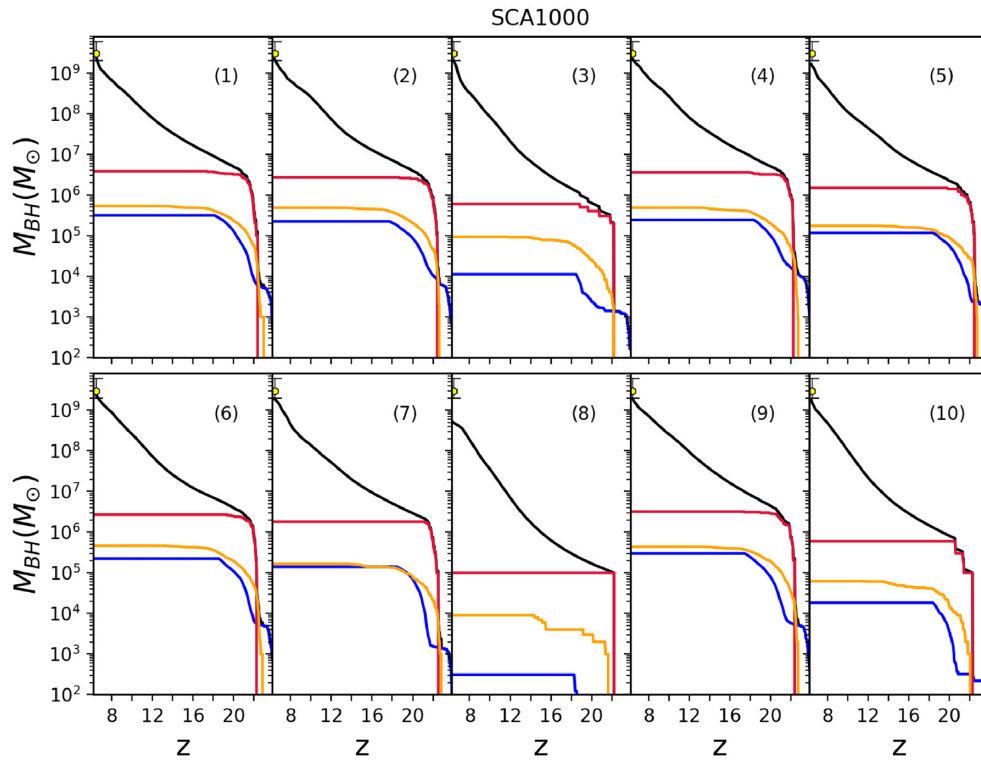


**Figure A4.** Same as Fig. A1 but for model SCA1000.

This paper has been typeset from a  $\text{\TeX}/\text{\LaTeX}$  file prepared by the author.